https://doi.org/10.5194/egusphere-2022-165
Preprint. Discussion started: 21 April 2022


# Use of fluorescent sand to assess plot-scale hydrological connectivity and sediment transport on young moraines in the Swiss Alps

**Fabian Maier[a*], Florian Lustenberger[a,b*] & Ilja van Meerveld[a]**

[a] Dept. of Geography, University of Zurich, Winterthurerstrasse 190, CH-8057 Zurich, Switzerland
[b] Swiss Federal Institute for Forest, Snow and Landscape Research WSL, Mountain Hydrology and Mass Movements, Zuercherstrasse 111, CH-8903 Birmensdorf, Switzerland

*These authors contributed equally to this work
Corresponding author: Tel.: +41 44 63 55232. E-mail address: fabian.maier@geo.uzh.ch.

**Keywords:** hydrological connectivity, transport distance, erosion, surface runoff, rainfall simulation experiments, photoluminescence

**Abstract**

The surface of the earth is constantly changing, especially in mountain areas, where glacial retreat uncovers large bodies of unconsolidated sediment. However, our knowledge on overland flow (OF) generation and related sediment transport is still limited, partly due to a lack of methods to trace the pathways of water and sediment on the surface. To investigate how different surface characteristics affect hydrological- and sediment connectivity on natural hillslopes, we studied five plots on two moraines of different ages in a proglacial area of the Swiss Alps. On all plots, we performed sprinkling experiments to determine OF characteristics, i.e., total OF, peak OF flow rate, peak turbidity and sediment concentrations, and total sediment yield. Here we test if a fluorescent sand tracer, together with UV lamps and a high-resolution camera, can be used to visualize the pathways of OF and to determine the typical sediment transport distances. The results highlight the ability of the setup to detect sand movement, even for individual fluorescent sand particles (300 – 500 µm grain size), and to distinguish between the two main mechanisms of sediment transport: OF-driven erosion and splash erosion. The experiments also revealed that the higher rock cover on the younger moraine enhanced surface hydrological connectivity and resulted in larger sediment transport distances. In contrast, the higher vegetation cover on the older moraine promoted infiltration and reduced the length of the surface flow pathways and erosion. The study, thus, demonstrates the potential of the new method to improve the observation of surface hydrological connectivity and sediment transport. These observations can help to improve our understanding of OF and sediment transport in complex natural settings.

https://doi.org/10.5194/egusphere-2022-165
Preprint. Discussion started: 21 April 2022


## 1 Introduction

Soil erosion rates in alpine regions are high (Panagos et al., 2015; Gianinetto et al., 2020; Musso et al., 2020a) and are expected to increase because of climate change. Rapid glacier retreat changes and exposes unvegetated areas that are prone to surface erosion, which increases sediment availability (Klaar et al., 2015) and the likelihood for debris-flows (Stoffel et al., 2014). Permafrost thaw is, furthermore, expected to decrease the stability of mountain slopes (Hock et al., 2019). These changes in glacier cover affect runoff and fish habitats (Carnahan et al., 2019; Cowie et al., 2014). Climate change is also expected to increase the frequency, intensity and amount of heavy precipitation (Anache et al., 2018; Hoegh-Guldberg et al., 2018; Nearing et al., 2004; Raclot et al., 2018, Maruffi et al., 2022), which can also affect erosion rates and sediment yield (Anache et al., 2018; Nearing et al., 2004). Splash erosion, i.e., the detachment of soil particles by the impact of raindrops, is positively correlated to rainfall intensity (Angulo-Martínez et al., 2012; Fernández-Raga et al., 2017; Park et al., 1983) because the larger raindrops during intense rainfall have a higher kinetic energy (Evans, 1980). If the rainfall intensity is higher than the infiltration capacity of the soil, infiltration-excess overland flow (Hortonian Overland Flow, HOF; Horton, 1933) occurs, which can transport the detached particles downslope, i.e., interrill erosion. Overland flow (OF) can also occur during long low intensity rainfall events when the soil becomes saturated (saturation-excess overland flow, SOF).

Whether OF can transport the detached particles to the bottom of a hillslope or a stream depends on the surface characteristics, and particularly the hydrological connectivity of the source areas to the slope bottom or stream, i.e., whether the two points are connected by water flow (Bracken and Croke, 2007; Smith et al., 2010). If water infiltrates into the soil after a short distance (i.e., the OF flow pathways are short), then the water and sediment it carries may not reach the bottom of the hillslope. Sediment connectivity thus depends on the amount and variability in OF, which is affected by the precipitation amount and intensity and the antecedent soil moisture conditions (Nanda et al., 2019), the spatial variability in infiltration rates (Vigiak et al., 2006; Gerke et al., 2015; Cammeraat, 2002), microtopography (Appels et al., 2016), and vegetation type and cover (Dunne et al., 1991; Thompson et al., 2010; Wainwright et al., 2000).

The importance of surface hydrological connectivity for sediment yield is well established (see e.g. Bracken et al., 2015; Heckmann et al., 2018; Najafi et al., 2021). Sediment connectivity has also been implemented in different conceptual frameworks (Brardinoni and Hassan, 2006; Heckmann and Schwanghart, 2013; Stock and Dietrich, 2003; Bracken et al., 2013; Bracken and Croke, 2007; Reaney et al., 2014) or explored in model studies (Appels et al., 2011; Reaney et al., 2014; Masselink et al., 2017; Peñuela et al., 2016). Other studies have defined hydrological and sediment connectivity indices to quantify the degree to which a system facilitates the transfer of water and sediment (e.g., Asadi et al., 2019; Gay et al., 2016; Heckmann et al., 2018; Lane et al., 2009; Shore et al., 2013; Zanandrea et al., 2021). However, little is known about the real-world connection of OF pathways (Wolstenholme et al., 2020) because it is difficult to observe connectivity and sediment transport during rainfall events, particularly for vegetated hillslopes. Connectivity of OF has been studied in arid areas (Smith et al., 2010; Moreno-De Las Heras et al., 2010; Lázaro et al., 2015), agricultural areas (Peñuela et al., 2016; Sen et al., 2010; Buda et al., 2009), and on frozen soils (Coles and McDonnell, 2018). Sen et al. (2010) analyzed runoff data from six natural rainfall events on pasture hillslopes and found that only well-connected areas with a low hydraulic conductivity produced OF during intense rainfall events. Wolstenholme et al. (2020) used visual observations of the OF pathways and highlighted the importance of infiltration along the flow path and flow resistance for the establishment of connectivity. They also stressed the importance of vegetation, slope, surface stone cover, and surface roughness for OF generation in dryland areas. Other studies compared flow below plots of different lengths (Gomi et al., 2008; Lázaro et al., 2015) or plots with and without an upper border (Buda et al., 2009) to infer connectivity and the maximum transport lengths.

Dyes and cameras (Polyakov et al., 2021; Wolstenholme et al., 2020; Smith et al., 2010; Gerke et al., 2015) and thermal imaging of heated water (Lima et al., 2015) have been used in rainfall simulation studies on laboratory flumes and in arid areas to determine OF distances and connectivity. Other studies used radio frequency identification tags (Parsons et al., 2014) or added rare earth element tracers (Polyakov and Nearing, 2004; Deasy and Quinton, 2010) or particles to the plots to study

https://doi.org/10.5194/egusphere-2022-165
Preprint. Discussion started: 21 April 2022


erosion and sediment transport. For example, Guzmán et al. (2015, 2010) used silt-sized magnetite, hematite, magnetic iron oxide, and goethite particle tracers mixed to soil aggregates to study sediment movement on agricultural fields. The tracer and sediment concentrations were measured in the runoff at the bottom of the plots but no observations were made on the plot surface to determine the actual flow pathways. Tauro et al. (2012b) used buoyant fluorescent polyethylene particles to determine particle flow velocities in OF on semi-natural hillslopes. They showed that Full HD videos (1920 × 1080 pixel resolution) were best for real-time detection for these rather large particles (1.0 – 1.2 mm). However, their fluorescent particles did not have the same shape as natural soil particles and had a different buoyancy (i.e., the particle could float on the water). Fluorescent sand can be used to overcome this drawback. Sand grains more closely represent the size and density of natural soil particles. Sand particles coated with a fluorescent paint were tested by Yasso (1966) and considered suitable for sediment transport studies. They have been used to track sediment movement on beaches (Ingle, 1966), along the surf zone in the Nile river delta (Badr and Lotfy, 1999), and to study on- and offshore sediment transport along the coast of Israel (Klein et al., 2007), as well as sand movement in a river tidal flat in Japan (Kato et al., 2014). Hardy et al. (2017 and 2019) used a fluorescent sand tracer with a similar particle size and density as the soil to study soil redistribution by tillage on arable farmland. They improved the early pioneer work of Young and Holt (1968), who used fluorescent glass particles to monitor sediment movement. However, fluorescent sand has so far not been used to determine rates of sediment movement on natural hillslopes (Parsons, 2019).

We, therefore, tested the use of a fluorescent sand tracer in combination with sprinkling experiments to study hydrologic connectivity and sediment transport on two young moraines in the Swiss Alps. The moraines differed in age and surface characteristics (e.g., vegetation cover, soil texture and aggregate stability, rock cover, saturated hydraulic conductivity and microtopography). More specifically, we assessed the following research questions:

- Can fluorescent sand particles be used to trace water and sediment on young moraines?
- How are the derived sediment transport distances related to the overland flow (OF) response (total flow, peak flow rate) and surface characteristics (vegetation cover, slope, surface roughness, saturated hydraulic conductivity, and soil aggregate stability)?
- Do the derived differences in sediment transport distances explain the differences in sediment concentrations and sediment yield?

We hypothesized that there would be more OF on the older moraine due to the lower infiltration rates (Lohse and Dietrich, 2005; Maier et al., 2020) but that erosion and sediment transport distances would be smaller for the older moraine due to the higher vegetation cover (Geißler et al., 2012). We, furthermore, expected that more microtopography would lead to a decrease in connectivity and sediment yield because of the larger depression storage and higher effective infiltration rates (cf. Govers et al., 2000). Finally, we expected that higher rainfall intensities lead to more OF and increased hydrological connectivity and sediment transport (Medeiros and de Araújo, 2013; Buendia et al., 2016; van De Giesen et al., 2000).

## 2 Site description

### 2.1 Study area

The field measurements were conducted between August and September 2018 in the forefield of the Steigletscher, south of the Sustenpass mountain road in the Central Swiss Alps (47°43' N, 8°25' E; Figure 1). The overall orientation of the forefield is north-northwest. The elevation ranges between 1800 and 2100 m above sea level (m a.s.l.). The mean annual air temperature (1991 – 2020) at the closest long-term automatic weather station (the Grimsel Hospiz, located 20 km from the study area at 1980 m a.s.l.) is 2.3 °C (MeteoSwiss, 2022). The average monthly temperature for the same period varies between -4.9 °C in February and 10.3 °C in August. The mean annual precipitation is 1834 mm $y^{-1}$. Precipitation is evenly distributed over the

https://doi.org/10.5194/egusphere-2022-165
Preprint. Discussion started: 21 April 2022


year, with frequent snowfall events even during the summer months. On average, there is more than 10 cm of snow on the ground for 210 days per year (MeteoSwiss, 2022). Even though streamflow is dominated by snow and glacier melt, high-intensity rainfall events are also important. The 30-minute rainfall intensity with a 10-year return period is 36 mm $h^{-1}$ (95 % confidence interval: 30 – 46 mm $h^{-1}$ (1990 – 2020 period; MeteoSwiss, 2021).

The study area is part of the internal alpine massif (Aarmassif) and underlain by the highly polymetamorphic "Erstfelder"-gneiss-zone. It predominantely contains biotite-plagioclase-gneiss, pre-mesozoic metagranitoids and amphibolites (Labhart, 1977). Based on glacier extend maps for the last 150 years and aerial images (Swiss Federal Office of Topography - 'Journey through time' - Map and 'SWISSIMAGE Journey through time' - Aerial Images), we selected two moraines that could be dated precisely (Figure 1). The older moraine originates from the ~~little ice age~~ (hereafter called 1860 moraine) and is approximately 160 years ~~in~~ age, while the younger moraine became ice-free in 1990 (hereafter referred to as the 1990 moraine) and is thus ~30 years old (c.f. Musso et al., 2020b; Maier and van Meerveld, 2021). Both moraines are located ~900 m north ~~from~~ the current terminus of the Steigletscher. The 1990 moraine is located ~30 m higher than the 1860 moraine. Both moraines are side moraines and are northeast-exposed.

Vegetation cover, root density and organic matter content are higher for the 1860 moraine than the 1990 moraine (Greinwald et al., 2021b). The 1860 moraine is largely covered by alpine sweet vernalgrass (Anthoxanthum alpinum), bellflowers (Campanula scheuchzeri), pale clover (Trifolium pallescens) and willow (Salix retusa and Salix glaucoserica) (Table 1). The 1990 moraine is dominated by fields of scree (Table 1) and pioneer plant species, such as pale clover (Trifolium pallescens), alpine bluegrass (Poa alpina) and alpine willowherb (Epilobium fleischeri) (Table 1). Typical early-successional communities on coarse-textured soils, such as Salix retusa and Salix hastata with shallow root systems (Hudek et al., 2017; Jonasson and Callaghan, 1992; Lichtenegger, 1996; Pohl et al., 2011) can be found on the 1990 moraine as well.

The soils of both moraines are sandy-loamy Hyperskeletic Leptosols and contain coarse gravel fragments, sand and buried stones throughout the profile (Musso et al., 2019). The soil texture in the upper 50 cm of soil is similar for the two moraines, with sand (particle diameter 63 µm – 2 mm) being the dominant particle size (~75 %; Hartmann et al., 2020a).

### 2.2 Study plots

On both moraines, we installed three bounded runoff plots, each with a size of 4 m by 6 m (Figure 1 & Table 1). To cover as much variability on each moraine as possible, we chose the location of the plots based on vegetation cover and functional diversity (Garnier et al., 2016; Maier et al., 2020; Greinwald et al., 2021b). More specifically, we selected on both moraines the area with the lowest (L), intermediate (M) and highest (H) vegetation complexity (Table 1; Maier and van Meerveld, 2021). The vegetation cover was 80, 80 and 95 % for the L, M and H plots on the 1860 moraine and 50, 30 and 45 % for the L, M and H plots on the 1990 moraine, respectively (Table 1, Figure 1). Because the 1860H plot was covered with dense shrubs of alpine rose that obscured the fluorescent sand, this plot was not included in any of the analysis (i.e., we report the results for five plots only). The plots had a comparable average slope, varying between 21° and 36° (Table 1). However, the topographic position of the plots differed. The 1860L, 1860M and 1990M plots are located at a mid-slope position, while the 1990L and 1990H plots are located at the bottom of the slope.

## 3 Methods

### 3.1 Plot characteristics

https://doi.org/10.5194/egusphere-2022-165
Preprint. Discussion started: 21 April 2022


#### 3.1.1 Topography and rock cover

A digital terrain model (DTM) derived from drone images of the moraines (drone: senseFly eBee; camera: Sony Cyber-shot DSC-WX220) was used together with the $D_\infty$ routing algorithm of Tarboton (1997) to determine the potential direction of OF in ArcMap (version 10.6.1). The drone-based images had a spatial resolution of ~4 cm, which was considered acceptable for the comparison with the results of the sediment movement (see section 3.3). For a better visualization of the plots and results, georeferenced photographs from a drone (DJI Phantom 4 Pro; see Figure 1) are used as a background in all plots because of their higher resolution. These images were also used to determine the rock cover for each plot based on a supervised classification using Adobe Photoshop (version CS6; tool: "color range").

The DTM was not used to determine the slope because of the coarse resolution and the distortion by the vegetation cover. Instead, the slope angle was determined based on twelve measurements with an inclinometer (every 50 cm at both sides of each plot). A 1.5 m long microtopography profiler, consisting of a wooden frame with 101 adjustable 1 m long metal rods (cf. Leatherman, 1987), was used on ten transects within each plot to determine the microtopography and surface roughness for each plot based on the normalized line length and the tortuosity index (Currence and Lovejoy, 1985; Bertuzzi et al., 1990). We report the average values for the measurements on the bottom half of the plots where the fluorescent sand and blue dye were applied (seven measurements for slope and six transects for microtopography).

#### 3.1.2 Soil aggregate stability

We determined the soil aggregate stability for six soil samples at each plot using the upper 10 cm of soil (collected using a HumaxTube®; GreenGround). We used the method defined by Bast et al. (2015), in which the soil sample is placed on a 20 mm sieve and submerged in water for 5 min. The aggregate stability coefficient (ASC) varies between 0 and 1, ranging from complete destruction of the soil sample to a fully stable soil sample (Bast et al., 2015). We report the median ASC-value for each plot (see also Greinwald et al., 2021a).

#### 3.1.3 Saturated hydraulic conductivity

Using a Double-Ring-Infiltrometer (inner diameter of 20 cm) we measured infiltration rates next to each plot at three locations (ASTM D3385-03 standard test method). The infiltrometers were inserted vertically into the ground by a minimum of 5 cm on all sides. The ponding depth was 15 – 25 cm. The saturated hydraulic conductivity ($K_{sat}$) was determined based on the steady-state infiltration rate (see also Maier et al., 2020; Maier and van Meerveld, 2021). We report the average value of the three measurements per plot. We acknowledge that many more measurements would be needed to obtain a robust average $K_{sat}$ value (e.g., Harden and Scruggs, 2003; Zimmermann, 2008), however, due to time limitations more measurements were not possible. Nonetheless, the six (1860 moraine) and nine (1990 moraine) measurements at each moraine already provide some information on the magnitude and variability in $K_{sat}$.

### 3.2 Rainfall and runoff measurements

#### 3.2.1 Plot set-up

At the left, right and upslope borders of each plot we ~~added~~ plastic sheets approximately 5 cm into the ground to reduce lateral in- and outflow of OF from the plots (Figure 2a). At the downslope border of each plot we ~~digged~~ a trench and inserted pond foil ~2 – 5 cm into the soil (Figure 2b). The foil was attached to a gutter, which was covered with plastic sheeting to protect it from the rain (Figure 2a). From the gutter, water flowed along a 5 cm diameter hose to an Upwelling Bernoulli Tube (Stewart

https://doi.org/10.5194/egusphere-2022-165
Preprint. Discussion started: 21 April 2022


et al., 2015), inwhich a pressure transducer was located (DCX-22-CTD, Keller). At each moraine one pressure transducer was installed as well to measure the local barometric pressure. By that the OF rate could be determined at a 1 min interval. The measurements of OF do also contain biomat flow (cf. Sidle et al., 2007) and very shallow subsurface flow because the pond foil was inserted into the soil up to 10 cm below the surface (Figure 2b; a more detailed description can be found in Maier and van Meerveld, 2021). However, we refer to this as OF throughout the remainder of this manuscript.

#### 3.2.2 Sprinkling experiments

On each plot, we performed three sprinkling experiments of different intensities over a three-day time period. We started with the lowest intensity experiment on day one and ended with the highest intensity experiment on day three (Table 2). We defined the three events as low intensity (LI), medium intensity (MI) and high intensity (HI) experiments. We used either one, two or three Senninger I-Wob adjustable sprinklers (nozzle number 22) to obtain the different intensities (Figure 2a). The sprinklers were placed at the center line of the plots at 2 m height (Figure 2a). The water was obtained from the nearby glacial stream and stored in two 4 $m^3$ water reservoirs, located more than 20 m above the plots to ensure sufficient pressure for the irrigation. From the reservoirs water flowed trough fire hoses, a water meter, and garden hoses to the sprinklers. We measured the actual rainfall intensities on the plots using two tipping buckets (RK400-04; Figure 2a) and at the plot boundaries using four manual rain gauges. For each experiment the actual rainfall intensities for the LI, MI and HI experiments varied (Table 2) because of wind drift and pressure differences. The average sprinkling intensities (± standard deviation) were 19±4 mm $h^{-1}$ (LI), 45±10 mm $h^{-1}$ (MI) and 65±20 mm $h^{-1}$ (HI). In each experiment rainfall was applied until the infiltration volume exceeded 20 mm. The infiltrated water was determined by subtracting OF from the applied rainfall. The average sprinkling durations were 68±8 min (LI), 45±9 min (MI) and 39±4 min (HI).

The area to which rainfall was applied by the sprinklers extended the plot dimensions, more specifically not less than 0.5 m upslope, several meters downslope and 4 m to the left and right. Based on the measurements of the actual sprinkled rainfall we determined the spatial uniformity of the applied rainfall (mean coefficient of variation of the measured rainfall 28±15 %; range: 9 – 48 %).

Using the oil method by Eigel and Moore (1983), we determined the median drop size at a rainfall intensity of 39 mm $h^{-1}$. The value of 1.2±0.4 mm (range: 0.4 – 2.7 mm) lies in the range for orographic precipitation (median drop size of 0.1 – 1.5 mm; Blanchard, 1953) and is very similar to the value for mountain regions in Western Europe (~1.1 mm; Hachani et al., 2017). We, hence, assumeed the kinetic energy of our rainfall simulation to be comparable to that of natural rainfall in the Swiss Alps. 24 hours before and between the experiments on one moriane we covered the plots with big tarps in case of natural occurring rainfall. As the topsoils drain approximately within 24 hours we set the intervals between the experiments on each plot to 24 hours. For coarse moraine soils, as e.g. on the 1990 moriane, the drainage is most likely even faster and, therefore, the hillslopes should have been close to field capacity for the MI and HI experiments. A slightly more extensive description of the experiments can be found in Maier and van Meerveld (2021).

#### 3.2.3 Suspended sediment measurements

To determine the sediment concentration in OF, 500 ml samples were taken from the outflow of the Upwelling Bernoulli Tubes. We started sampling with the start of the outflow and continued after the experiment ended until the outflow stopped. More samples were taken on the rising limb than on the falling limb. To determine the amount of sediment per sample we used 1.6 µm filters (GF/A Whatman). For a more detailed description see Maier and van Meerveld (2021).

A Cyclops 7 turbidity probe (Turner designs) was installed between the gutter and the Bernoulli Tube (Figure 2a) and measured the turbidity of OF every minute. The turbidity at the time of sampling was related to the sediment concentrations to obtain

https://doi.org/10.5194/egusphere-2022-165
Preprint. Discussion started: 21 April 2022


the relation between turbidity and suspended sediment concentration. This was done separately for each moraine. The coefficient of determination ($R^2$) for this relation was 0.80 for the 1860 moraine and 0.89 for the 1990 moraine. The regression slope was 3.1 mg $L^{-1}$ $NTU^{-1}$ for the 1860 moraine and 3.3 mg $L^{-1}$ $NTU^{-1}$ for the 1990 moraine. These values are comparable to those reported for alpine streams (Paschmann et al., 2017; Geilhausen et al., 2013; Orwin et al., 2010). We used these correlations and estimated suspended sediment concentrations with a high temporal resolution. Finally, the suspended sediment yield was determined for each event by taking the sum of the products of the OF rates and the suspended sediment concentrations that were estimated at the same point of time (see also Maier and van Meerveld, 2021). On the 1990 moraine, some sediment was trapped in the Bernoulli Tubes and was not sampled. Thus, the sediment yield might be slightly higher than estimated.

### 3.3 Fluorescent sand transport

#### 3.3.1 Field set-up

Before each sprinkling experiment, a line of fluorescent sand (Noxton™; Glow in the Dark Sand) was applied to the soil surface in the middle or lower half of the plot (Figure 2c). The quartz sand is coated with a non-toxic, photoluminescent (fluorescent and phosphorescent), non-dissolvable powder (TAT33), containing $CaAl_2O_4$ and $Al_2O_3$ (Material safety data sheet of glow in the dark powder TAT 33). After illumination, the sand has an afterglow for several minutes. The particle sizes of 300 – 500 µm corresponds well with the grain size on the 1860 and 1990 moraines (median: 82 and 76 % sand content (particles between 2 mm and 0.063 mm)) for the top 10 cm of the soil (Hartmann et al., 2020b; Musso et al., 2019). We used three different colors of fluorescent sand (orange for LI, green for MI and blue for the HI experiments). We chose to apply the sand to the lower half of the plot because OF is more likely to occur there due to the larger contributing area). The applied sand ribbons were about 3 to 5 cm wide, 2 cm thick, and 1.5 m long on the 1860 moraine and 3.1 m long on the 1990 moraine.

#### 3.3.2 Photographs

Pictures of the fluorescent sand were taken before and after each sprinkling experiment. A red-white 0.5 m segmented fluorescent plastic chain (Novap) was installed around the bottom half of the plot and served as a reference marker during the image analysis later. In addition, thin red fluorescent ropes were placed every 0.5 m across the plot (Figure 2a, c) and served as approximate distance markers. In the nights before and after the sprinkling experiments, the fluorescent chain, ropes and sand were illuminated for ~10 min with six 18 W UV lamps (Eurolight). Four lamps were mounted on a pole that was installed over the plot (Figure 2c) and two were handheld to illuminate areas in the shadow. These lamps emit light in the ultraviolet (UV) range at around 365 nm. The sand was additionally illuminated for ~10 min with two 23 W LED lights in order to activate the sands afterglow. The LED light panels were moved to different positions around the plots to illuminate the areas in the shadow as well.

A camera (Sony Alpha 7R II) with a wide-angle lens (Sony Vario-Tessar® T* FE 16 – 35 mm F4 ZA OSS) was mounted on a tilting angle (to account for the average slope of the plots) on a 4 m high tower below each plot (Figure 2a). This camera was used to take photos of the sand ribbons during UV illumination. The photos were saved with full pixel resolution (42 megapixels) in the RAW-format (.ARW file) to obtain a high-quality image with maximum dynamic range, as well as in the JPEG-format for faster post-processing. The aperture was set to fully open (F/4). During windy nights, the camera tower moved slightly, which led to blurry photos when high shutter speeds were chosen. Thus, during windy conditions, the shutter speed was set to one second and higher ISO values (up to 8000) were used instead. During nights with little wind, the shutter speed was set to two, five or ten seconds to reduce the ISO to 1000 – 5000 (depending on the light conditions) and obtain better quality pictures.

https://doi.org/10.5194/egusphere-2022-165
Preprint. Discussion started: 21 April 2022


On the 1990L plot, we additionally used a brilliant blue dye tracer solution during the MI and HI experiments to visualize the water flow pathways. We manually added the blue dye tracer to the surface at places where OF was visible. The flow paths of the dye tracer were recorded on video in Ultra HD resolution (3840 × 2160 pixels) with 25 frames per second using the camera (Sony Alpha 7R II) that was installed on the camera tower. The combination of several video frames led to a composite picture of the flow path networks on the surface, which could then be compared to the movement of the fluorescent sand.

#### 3.3.3 Image pre-processing

The photos of the sand ribbons were post-processed to obtain a matrix for each photo where each element corresponds to 1 pixel with an area of 1 $mm^2$ on the plot containing and has a value of one if there was fluorescent sand and zero if there was no sand. These matrices are called classified images in the remainder of the text (Figure 3b). The procedure used to classify the images is similar to a supervised classification algorithm in remote sensing analyses (e.g., Richards, 2013).

All photos were geometrically corrected using the segmented chain around the plot as a spatial reference in Python (v3.8.8 – used with the Scientific Python Development Environment (Spyder) v4.1.5), so that each pixel corresponded to 1 $mm^2$ (cf. Schneider et al., 2014; Weiler, 2001; Weiler and Flühler, 2004). The areas outside the plots were cropped with Adobe Photoshop CC 2021 (v22.2; Figure 3a). The detection of the sand particles was done in the hsv (hue, saturation, value) color space which has the advantace that a single number (hue) represents the color. If the hue of a pixel was in the specified range for the sand and the value (v) was above 10 %, then the pixel was classified as fluorescent sand. We chose at least ten representative locations on each sand ribbon to determine the typical hue of the sand in Adobe Photoshop (orange: 0° – 80° and 320° – 360°, green: 150° – 180°, blue: 180° – 240°). As the sand had a certain brightness (due to its afterglow) a value (v) of at least 10 % was chosen to reduce misclassifications in the dark parts (e.g., due to reflections on rocks etc.). The classification was done in Python, based on the script for detecting a brilliant blue dye tracer in soil profiles (Weiler, 2001). To detect the orange sand, the segmented chain and the fluorescent ropes had to be manually removed in Adobe Photoshop because their hue was in the same range as the sand. To detect the blue sand, the green sand had to be manually removed in Adobe Photoshop because some green sand particles had a hue within the typical blue sand hue range (i.e., a hue > 180°).

#### 3.3.4 Image analysis

The fluorescent segmented chain around the plot became slightly bent during the experiments (due to its weight). Therefore, the reference points for the geometric correction differ for the pre- and post- experiment classified images (i.e., the matrix coordinates (0, 0) in the pre- and post experiment classified images do not have the same position on the plot). This means that the pre- and post classified images cannot be overlaid. Therefore, a theoretical starting line at approximately the middle of the sand ribbon was defined for all classified images (pre- and post-experiment, cf. Figure 3c). The assumption is that the main part of the sand ribbon did not move during an experiment and only individual sand particles and clusters moved (i.e., the position of this starting line along the middle of the sand ribbon did not change during an experiment). Based on the starting lines from the classified images, a relative measure from where the sand moved can be calculated to determine the sand distance.

More specifically, the starting line in each classified image (pre- and post-experiment) was defined as follows. For every point along the slope (i.e., each individual pixel column in the classified image), we determined a window of 101 pixels wide (50 pixels on each side, representing a 10.1 cm wide section of the plot) and counted the number of pixels that were classified as sand for each row (i.e., every 1 mm upslope from the gutter) within this window. The row with the highest number of classified pixels was considered the starting line for this column and thus the starting point of sand movement. In case there were several maxima, the median row height was taken as the starting point. If there were only a few (< 30) classified pixels, the value from

https://doi.org/10.5194/egusphere-2022-165
Preprint. Discussion started: 21 April 2022


the neighboring column was used to avoid breaks in the starting line for the sand ribbon (i.e., there were no gaps in the starting line, even if the sand ribbon itself had a small gap). At the left and right borders of the plot, the moving window was shorter to account for the lack of neighboring points on one side.

We did not use the maximum distance that the sand moved from the starting line as a measure for sand movement because it is very sensitive to the detection of individual sand particles. Furthermore, it would not account for the transport of the sand off the plots (i.e., into the OF gutters). Instead, we used two measures: one related to the distance that the sand moved on the plot (ΔD) and the other to the area over which the sand moved (ΔA). For each point along the plot (i.e., each column i in the classified images), we determined the distance ($x_i$) between the starting line and the lowermost pixel that was classified as sand (Figure 4). We did this for the classified images taken before and after the experiments. The average value of this distance for the classified image taken before the sprinkling experiments indicates approximately half of the width of the sand ribbon. Any change in this average distance for the classified image taken after the experiment is an indication for sand movement, assuming that not the entire sand ribbon moved downwards (which we indeed did not observe). Because the sand did not move at most points along the slope, we put extra weight on the particles that were located far from the starting line by using the root of the mean squared maximum distance for each column ($x_i$):

$$D = \sqrt{\frac{1}{n} * \sum_{i=1}^{n} x_i^2} \qquad \text{Equation 1}$$

where i represents the location along the slope (i.e., the column number in the classified image) and n the total number of pixels along the plot (i.e., the total number of columns). To calculate how the mean root squared distance D changed from before to after the experiments and thus to obtain a measure of the distance that the sand moved during an experiment, the percent change in D (ΔD) was calculated:

$$\Delta D = \left(\frac{D_{after}}{D_{before}} - 1\right) * 100\ \% \qquad \text{Equation 2}$$

where $D_{after}$ is the root of the mean squared distance of the sand after the sprinkling experiment and $D_{before}$ is the root of the mean squared distance of the sand prior to the sprinkling experiment, and ΔD represents the percent change in the root of the mean squared distance (increase or decrease in %).

As a measure of the spread of the sand, we also determined the potential area over which the sand moved (A; Figure 3d and 4c). Specifically, we selected all pixels between the furthest downslope and upslope occurrence of sand for each column of the classified images. Sand particles located more than 20 cm above the starting line were not considered to determine the area as they are most likely not part of the sand ribbon. To account for the fact that the sand particles did not move down the hillslope in a straight line, in each column the uppermost and lowermost (i.e., furthest upslope and downslope) occurrence of sand was calculated for a 41 column window (i.e., 20 columns on each side, representing 2 cm on the plot; Figure 4). In case of gaps in the sand ribbon, the interpolated starting line was used to merge all areas to one area (Figure 4). Similar to the calculation of the sand travel distances, the percent change in the area A (ΔA) was calculated (Eq. (2) but with the A instead of D) to determine the change in the area over which the sand was spread during the sprinkling experiments. This ΔA does not represent the actual area over which the sand moved during the experiments (and would likely overestimate this) but is used here as a measure to compare the spreading of the sand for the different experiments and plots.

### 3.4 Data analysis

To determine if the differences in the surface characteristics for the five plots were statistically significant, we used the Kruskal-Wallis tests and Nemenyi post-hoc tests. To determine if the differences in the surface properties or OF and sediment responses were significantly different between the two moraines, we used the Mann-Whitney test.

We used Spearman rank correlation to determine the correlation between the surface characteristics and the OF characteristics

https://doi.org/10.5194/egusphere-2022-165
Preprint. Discussion started: 21 April 2022


(total overland flow and peak flow rate), sediment yield and peak turbidity. We, similarly, used Spearman rank correlation to describe the relation between the surface-, OF- and rainfall characteristics and the percent changes in sand distance (ΔD) and sand-covered area (ΔA). ~~We, furthermore,~~ used a multiple linear model with the rainfall intensity as additional variable to identify the interaction between rainfall intensity and the most plot characteristics for OF and sediment yield. For the analyses, we used a 0.05 level of significance and the software R (v4.0.5 – used with RStudio v1.4.1106), especially the packages: "stats", "caret" "PMCMRplus", "rsq" and "ggplot2".

## 4 Results

### 4.1 Plot characteristics

#### 4.1.1 Slope and microtopography

All of the plots were relatively steep (median: 27°), ranging from 18° on 1990L to 35° on 1860M (Table 1; Figure 5a) but the plots on the 1860 moraine were on average steeper than the 1990 moraine (29° vs. 26°). The differences between the median slopes of the plots (p = 5e-04) and the two moraines (p = 4e-03) were significant. The variability in the slope was largest for the 1990L plot and smallest for the 1990M plot (coefficient of variation (CV) of 0.41 and 0.16, respectively).
There was also a significant difference in the microtopography between the plots (p = 0.01; Figure 5b) and the moraines (p = 7e-03). The tortuosity index increased significantly from the 1860 moraine (median: 0.32; range: 0.18 – 0.47) to the 1990 moraine (median: 0.39; range: 0.26 – 0.86). The variability in the tortuosity index values was largest for the 1860M plot and smallest for the 1990M plot (CV of 0.32 and 0.15, respectively).

#### 4.1.2 Soil aggregate stability

The aggregate stability of the top 10 cm of the soil (Figure 5c) was ~~statistically significant~~ between the plots (p = 0.02; Figure 5c) and decreased significantly from the 1860 moraine to the 1990 moraine (p = 2e-03). The median soil aggregate stability coefficient (SAC) was lowest for the 1990M plot (0.14) and highest for the 1860M plot (0.71). The variability in soil aggregate stability was largest for the 1990M plot and smallest for the 1860L plot (CV of 0.74 and 0.44, respectively).

#### 4.1.3 Saturated hydraulic conductivity

The saturated hydraulic conductivity ($K_{sat}$) of the soil surface (Figure 5d) was not significantly different between the five plots (p = 0.1). The median values ranged between 1320 mm $h^{-1}$ (1860M) and 6120 mm $h^{-1}$ (1990M). The median $K_{sat}$ was significantly lower for the 1860 moraine than the 1990 moraine (median values of 1560 mm $h^{-1}$ and 4320 mm $h^{-1}$, p = 0.04).

### 4.2 Overland flow, turbidity and sediment yield

OF was less frequently observed on the 1860 moraine (three of the six experiments) than on the 1990 moraine (seven of the nine experiments, Figure 6 & Table 2). OF was not observed for any of the low intensity (LI) experiments on the 1860 plots but was observed for all high intensity (HI) experiments on these plots. The runoff ratio (total OF divided by total precipitation) was < 3 % for each moraine, except for the 1990L and 1990H plots that were located at the footslopes of the moraines and for which it was 10 and 8 %. The average OF amount (for all experiments on a moraine) was almost three times larger for the 1990 moraine (1.8 mm) than the 1860 moraine (0.7 mm). For the HI experiments, this difference was smaller (2.6 mm for the

https://doi.org/10.5194/egusphere-2022-165
Preprint. Discussion started: 21 April 2022


1990 moraine vs. 1.5 mm for the 1860 moraine). The total amount of OF was especially high for the 1990L plot (3.6 mm during the HI experiment; 8.1 mm in total for all three experiments; Figure 6).

Peak turbidity and sediment yield increased with rainfall intensity and were highest during the HI experiments for the 1990L and 1990H plots located at the foot of the moraines. There was a significant positive correlation between the peak flow rate and peak turbidity (Figure 7a), as well as between the amount of OF and sediment yield (Figure 7b). For the 1990H plot, the total OF amount did not increase from the low to high-intensity experiments, but sediment yield did. For the plots on the 1860 moraine, peak turbidity and total sediment yield were small (Figure 6).

### 4.3 Sand movement

#### 4.3.1 Patterns of sand movement and changes in sand-covered areas

Individual sand particles and small clusters of sand (< 1 $cm^2$) were detected below the sand ribbon on both the 1860L and 1860M plots after the sprinkling experiments (Figure 8). For the 1860L plot, sand movement was more widespread during the high intensity HI experiment (blue sand ribbon) than for the other experiments, as reflected by the larger areas covered by the sand for the HI experiment than the LI and MI experiments. Such large sand-covered areas were also observed for the 1990L and 1990M plots (Figure 8). For the 1990H plot, individual sand particles, small clusters and larger sand-covered areas were detected below the sand ribbons. However, compared to the 1990L and 1990M plots, hardly any sand moved on the 1990H plot. These qualitative differences in sand movement between the moraines are reflected in the differences in the sand travel distances $\Delta D$ ($p = 3e\text{-}03$) and sand-covered areas $\Delta A$ ($p = 2e\text{-}03$; Figure 9 and Table 2).

For five of the six experiments on the 1860 moraine, the change in sand-covered area was negative (i.e., it decreased); the sand travel distance was negative for four of the six experiments. Such decreases were not observed for the experiments on the 1990 moraine (Figure 9). The decrease was largest for the LI experiment on the 1860L plot ($\Delta D$: -51 % and $\Delta A$: -52 %); the largest increases were observed for the 1990L plot (Figure 9).

#### 4.3.2 Comparison with the blue dye

The flow pathways of the brilliant blue dye tracer matched the distribution of the sand-covered areas well (Figure 10a and b). Sand and OF moved in four distinct areas on the 1990L plot, which matched the flow patterns derived from the DTM (Figure 10c). The first flow path (#1 in Figure 10) was towards the left plot boundary (when looking upslope). The orange sand placed on the plot before the LI experiment was redistributed along this flow path. The second OF flow path (#2 in Figure 10) was downwards and slightly to the left. Sand particles from all three sand ribbons were found here, suggesting that OF occurred here during all three experiments. The third pathway (#3 in Figure 10) is mainly characterized by ponding in the slightly flatter area of the plot. In this microtopographic depression, the blue sand from the HI experiment was deposited. A fourth OF pathway (#4 in Figure 10) was observed during all experiments and all three sand colors were found in this region.

### 4.4 Relation between overland flow, sand movement and plot characteristics

There was no significant correlation between the percent changes in sand-covered area and either the total amount of OF, peak OF rate, peak turbidity, or sediment yield (Figure 11a – d). This was mainly due to the fact that for some experiments, no OF was measured at the bottom of the plot but there were changes in the sand-covered area. If these events are excluded from the analyses, a higher percent change in the sand-covered area corresponds to more OF, a higher peak OF rate, peak turbidity or sediment yield (Figure 11a – d). Relations for the sand travel distance were similar (see Figure S11 in Supplementary Material).

https://doi.org/10.5194/egusphere-2022-165
Preprint. Discussion started: 21 April 2022


The percent change in sand-covered area (p = 7e-04) was significantly positively correlated to the surface rock cover, similar to the total amount OF (p = 7e-03) and sediment yield (p = 0.01). The percent change in sand-covered area (p = 0.03) and total amount of OF (p = 0.04) were also significantly positively correlated to the microtopography (i.e., tortuosity index). The percent change in sand-covered area was also negatively correlated to the vegetation cover (p = 0.03) and $K_{sat}$ (p = 0.01).

The Multiple Linear Model indicated that rock cover, vegetation cover and ~~that~~ their interaction with the rainfall intensity could predict the total OF ($R^2$ = 0.64; Root Mean Squared Error (RMSE) = 0.6 mm) and sediment yield ($R^2$ = 0.77; RMSE = 5.2 g) but these plot characteristics were not very suitable predictors for the percent changes in sand-covered area ($R^2$ = 0.35; RMSE = 70 %).

# 5 Discussion

## 5.1 Evaluation of the fluorescent sand method

### 5.1.1 Advantages and disadvantages of the fluorescent sand to study soil erosion

The results of our study suggest that fluorescent sand is a valuable method to assess surface hydrological flow paths and connectivity as well as sediment redistribution on natural hillslopes with coarse soils and little vegetation (Figure 10). In particular, it provides information on the movement of particles inside the plot, flow pathways and travel distances. The main benefit of the sand tracer method is that very local and short sediment movement is identifiable. Thus, some information on OF and soil erosion can be obtained, even if no OF is detected below the plots. For example, for several experiments on the 1990M plot, there was considerable sediment movement, even-though no OF was recorded. This would not have been observed based on sediment measurements at the bottom of the plot (and explains the lack of the correlation between sediment yield and sand movement (Figure 11d). The fluorescent sand also provides information on the locations of infiltration of OF and deposition of the sediment, and thus the identification of local sinks. The disadvantage is that it is difficult to use the measurements of local movement of fluorescent sand particles to predict sediment yield at the bottom of the plot. For sediment yield, the particles need to travel at least to the bottom of the plots. This was not the case for several of our experiments.

Another main advantage is that it can be used to study sediment transport during natural rainfall events (although we didn't do this). Previous studies to detect OF pathways required real-time observations of the water or the tracer. To automate data collection during the event, they measured water temperatures with thermal cameras (Lima et al., 2015) or recorded videos for particle detection on beaches, rivers, or hillslopes (Tauro et al., 2012a, b, 2016; Hardy et al., 2017, 2016). This requirement for photographs or videos during the event means that the tracer can only be used during sprinkling experiments or at places where the timing of sediment transport is predictable (e.g., the beach). The advantage of the fluorescent sand method is that it does not need a real-time particle detection or tracking system. It means that the particles can, at least in theory, be applied to a surface and photographs can be taken before and after the next rainfall event, so that fully natural conditions can be studied. However, despite being listed as waterproof, the sand formed aggregates (1 – 15 mm in size) after a wetting and drying cycle, most likely because parts of the glue that bond the photoluminescent tracer powder on the sand particles were dissolved. In the following sprinkling experiments, such aggregates were hardly broken up and were thus more difficult to be transported. As a result, the sand particles that we used~~,~~ can only be used to determine sediment transport for the first event after application. This is a disadvantage because it requires application before the event of interest but also means that there is more time available to take the photographs afterwards.

The fluorescent sand method is well suited to study sediment transport on poorly vegetated soils that contain a significant amount of sand (i.e., have a similar grain size as the sand tracer). In other words, it is well suited for coarse hillslopes in high alpine regions, dune soils, etc. However, the sand does not move exactly like the soil. The fluorescent sand was loosely distributed in the form of sand ribbons over the plots and did not represent the natural aggregates of soil particles and their

https://doi.org/10.5194/egusphere-2022-165
Preprint. Discussion started: 21 April 2022


stability, even if the size of the fluorescent sand agreed well with that of the topsoil, particularly for the 1990 moraine. On soils with finer textured material, the method will no longer represent the transport of the natural soil particles but may still be useful to indicate the main pathways of OF. We consider the method applicable from the microscale (several centimeters) to hillslope scales (several meters) but do not recommend applying it to larger scales because the image resolution becomes too coarse. Also, not all of the sand movement can be attributed to OF-driven soil erosion. The different patterns of sand movement (isolated small clusters, aggregates or even single sand particles vs. more connected parts covered by fluorescent sand) indicate the influence of splash erosion as an additional transport mechanism. Recorded maximum splash distances for sand particles in the range of the fluorescent sand used in this study (300 – 500 µm) are ~45 cm for rainfall intensities of ~30 mm $hr^{-1}$ and a median raindrop size of ~1.4 mm (Legout et al., 2005). This agrees well with the observed maximum sand travel distance ranges of this study (0 – 1320 cm), especially considering that sand particles can be moved by splash erosion multiple times.

### 5.2 Impacts of surface characteristics on overland flow and sand movement

Although the focus of this study was mainly on the applicability of the fluorescent sand and not on the relations between the surface properties, OF generation and sediment transport, and the results have to be interpreted with caution as the number of experiments and observations was very small, they provide us with interesting results regarding OF generation and sediment transport on moraines of different ages. The significant differences in the total amount of OF and runoff ratios between the 1860 and 1990 moraines (Figure 6) imply a difference in the partitioning of rainfall into overland flow (OF) and infiltration. The substantially higher OF on the 1990 moraine and the results of the multiple linear model suggest that the high rock- and stone cover led to considerable OF generation, even-though the $K_{sat}$ values for the topsoil were high (and higher than for the 1860 moraine). This is in agreement with several studies that have reported quicker and more pronounced OF responses on hillslopes with large rock- and stone cover (Lavee and Poesen, 1991; Poesen et al., 1990; Poesen and Lavee, 1994). The rocks and stones on the 1990 moraine are also responsible for the larger microtopography. Some studies have shown that a high surface roughness can reduce hydrological and sediment connectivity and provide sinks that retain OF, increase infiltration and prevent further downslope flow (Thompson et al., 2010a; Dunkerley, 2003; Johnson et al., 1979; Jomaa et al., 2012). However, other studies (e.g., Darboux and Huang, 2005; Dunkerley, 2004; Helming et al., 1998) have reported a positive correlation between ~~microtopography~~, OF generation and hydrological connectivity because the surface roughness concentrated the flow and accelerated flow of water in downslope-orientated structures. This flow in rills can promote sediment transport and enhanced erosion (Liu and Singh, 2004). We assume that this was the case for the plots of the 1990 moraine, where the OF pathways (as visualized by the brilliant blue dye) indeed followed microtopographic depressions with a downslope orientation (Figure 10). The strong overlap between the redistribution of the fluorescent sand (sand polygons) and the pathways of the brilliant blue dye allows the identification of the surface areas that promote the generation of OF and the re-infiltration of this OF (Figure 10). The surface areas covered with rocks and stones (Figure 8, Figure 10 and Figure S12 in Supplementary Material) prevent infiltration of the rain and infiltration of the OF that was generated further uphill. In slightly flatter areas, the water may infiltrate and the sand particles were deposited.

In contrast, the plots on the 1860 moraine are characterized by a smooth surface, dominated by grassland vegetation, with denser root networks and macropores close to the surface that promote infiltration (Hino et al., 1987; Ding and Li, 2016). The rock- or stone cover could not promote OF and the transport of sediments was largely absent (Figure 1 and Table 1). On these plots, most sand polygons were small and part of the sand disappeared during the experiments (Figure 8, Figure 9 and Table 2), which suggests vertical transport (translocation) of the sand particles into the root channels of the macroporous topsoils, or at least below the vegetation. Vegetation cover and plant roots also protect soil particles from detachment (Geißler et al., 2012; Gyssels et al., 2005) and act as barriers that trap eroded sediment (Wainwright et al., 2000; Rey, 2003; Pearce et al., 1997). The negative values for ΔD and ΔA for the plots on the 1860 moraine are, thus, mainly caused by the higher vegetation cover

https://doi.org/10.5194/egusphere-2022-165
Preprint. Discussion started: 21 April 2022


compared to the 1990 moraine (cf. Ebabu et al., 2018; Marques et al., 2007; Mu et al., 2019; Rey et al., 2004; Zhang et al., 2004). The transport of the fluorescent sand below the ribbons (Figure 8), however, also highlights that even if no OF is measured at the bottom of the plot (Figure 6), there may be local OF and transport of sediment on the plots (Figure 8, Figure 9) but that connectivity to the bottom of the plot is low.

The difference in total OF amount explains the observed differences in sediment yield (Figure 6, Figure 7b) and the redistribution of the fluorescent sand (Figure 8 and Figure 10). The plot with the most OF also had the largest overall sediment yield (1990L). This is not surprising as the importance of OF for soil erosion has been recognized for decades (e.g., Farmer, 1971; Knapen et al., 2007; Komura, 1976; Parsons, 1992; Poesen, 2017; Singer and Walker, 1983). The importance of the surface characteristics and microtopography for OF generation and sand movement is also reflected in the similar correlations and the multiple linear model. The positive, rather than negative, correlation between the $K_{sat}$ and sediment transport is because $K_{sat}$ was measured for the sediment between the rocks, not the impermeable areas of the surface rocks. Surface infiltration on the 1990 moraine is much lower than on the 1860 moraine due to the high rock cover, despite the higher $K_{sat}$ for the sediment between the rocks.

#### 5.2.1 Uncertainties of the method and suggestions for improvements

The use of the fluorescent segmented chains around the plots was sub-optimal, as they did not stay in the exact same position during the experiments. Due to their own weight, they slightly bent towards the plot area. Additionally, the chains did not allow to work with distinct tie points. This limited their use for geometric correction of the photos as no tie points, but rather tie areas were visible. However, such tie points are essential for a proper geometric correction, as they define the rescaling of the photo (see also Weiler and Flühler, 2004).

The 42 megapixels resolution of the photos with (7952 × 5304 pixels) was very good (on the plot surface 1 pixel corresponds to a length of about 0.5 – 0.7 mm) and allowed for the detection of individual fluorescent sand particles. Bringing the resolution down to 1 $mm^2$ per pixel after the geometric correction of the photos led to a spatial resolution that was comparable to other plot-scale studies (Hardy et al., 2017, 2019).

The experiments could have been performed during daylight, leading to easier working conditions. Also, we used no wavelength filters (as e.g., Hardy et al., 2019) because of the need for common rgb photos for visual comparisons (e.g., with the brilliant blue tracers), which makes the method even easier. The detection of the sand would also be possible without the use of LED-lamps or with a common fluorescent tracer (without self-glowing abilities) instead (as used by Hardy et al., 2019, 2017, 2016; Tauro et al., 2016, 2012a, 2012b; Young and Holt, 1968). However, the use of a glow in the dark sand that still emits light after several minutes without a light source is a considerable advantage for very rough surfaces, where vegetation or rocks lead to shading and some of the sand particles cannot be seen directly. By moving the LED-light sources around the plot before taking the photos, it was possible to see these particles due to their after-glow. On young moraines where the surfaces are rough, this is particularly useful.

The hue of the green and blue sand was not optimal as their color range overlaps at around 180° (green: 150° – 190°, blue: 180° – 240°). Thus, parts of each colored sand (around 180°) was not classified correctly as the color detection ranges were set to be unique (green: 150° – 180°, blue: 180° – 240°). This is no issue if only one sand color is used. For a better separation and a distinct classification, sand colors with gaps between their hue detection ranges should be chosen, meaning that one should either use a brighter green or a darker blue. Furthermore, we found that the blue color was more easily washed off the sand particles than the green and orange color, which led to more white, non-glowing, and, thus, undetectable sand particles.

However, the sand particle classification based on a defined hue range per sand color in the hsv color space was successful. The sand ribbon, small sand clusters and even individual sand particles could be detected (cf. Figure 3a and b). We had to assume that the main part of the sand ribbons did not change from the pre- to post-experiment photos, which leads to some

https://doi.org/10.5194/egusphere-2022-165
Preprint. Discussion started: 21 April 2022


uncertainty in the percent changes of the sand distances (ΔD). However, we assume that this uncertainty is small, also because we used the root of the mean squared values. Furthermore, the agreement between the percent changes in the distances and areas suggests that both metrics can be used to characterize sand transport.

## 6 Conclusions

We describe a novel method (i.e., fluorescent sand) to study overland flow (OF) pathways, sediment transport and connectivity on moraines in the Swiss Alps. The fluorescent sand was applied prior to sprinkling experiments to (i) assess the usefulness of the method to reconstruct OF pathways and the related sediment transport distances, and (ii) evaluate how different surface properties (cf. differences in soil characteristics, vegetation- and rock cover and microtopography) affect the flow of water and distribution of sediment.

The results show the feasibility of using LED and UV lamps and a high-resolution camera to take pictures at night before and after the rainfall event to quantify the movement of fluorescent sand particles (300 – 500 µm) and to identify sediment transport. A main advantage of the fluorescent sand as a tracer is that it shows the redistribution of sediment on the plot, even if no OF is observed at the bottom of the plots and that no photos or videos need to be taken during the experiment. The comparison of the photos taken before and after the sprinkling experiments showed that the fluorescent sand was mainly transported to distinct areas and that these areas agreed with the flow pathways of the overland flow, as observed during dye staining experiments. The photos also highlighted the differences in sediment transport for the two moraines. The more extensive vegetation cover on the older 1860 moraine presumably provoked more infiltration into near-surface macropores and preferential flow paths. At the same time, it protected surface particles from rain splash detachment and transport. In contrast, the high rock cover on the younger 1990 moraine increased microtopography and reduced surface infiltration rates, leading to concentrated OF pathways and larger sediment transport distances, and for some experiments, a high sediment yield.

## 7 Code and data availability

The data described in this article and the developed codes are available on request at the first corresponding author.

## 8 Author contribution

IvM came up with the idea and formulated the overarching research goals, together with FM and FL. IvM, FM and FL developed the idea for the methodology and the design of the study. FM and FL performed the fieldwork and collected the data. FL was responsible for the fluorescent sand photography and analysis. FM and FL wrote major parts of the manuscript and the codes and IvM reviewed and edited the original draft of the manuscript. FM and FL produced all figures. IvM provided the funding of the study and large parts of the field materials, laboratory equipment and computing resources.

## 9 Competing interests

The authors declare no competing interests.

https://doi.org/10.5194/egusphere-2022-165
Preprint. Discussion started: 21 April 2022


## 10 Acknowledgements

This research was funded by the Swiss National Science Foundation (SNSF; project grant number 200021E-167563/1) and the German Research Foundation (DFG; project number 318089487) and is part of the HILLSCAPE project (www.hillscape.ch). We are commercially and financially independent from Noxton Technologies™.

We thank all members of the HILLSCAPE team, including the MSc. students, BSc. students, interns and staff who were involved in the data collection. We, furthermore, thank the Alpin Center Sustenpass, and in particular Thomas Michel, for logistical support, meals and accommodation during the fieldwork. Many thanks to Peter Luchs and the Kraftwerke Oberhasli AG for the permission to conduct fieldwork on their property and the provision of tools.

## 11 References

Anache, J. A. A., Flanagan, D. C., Srivastava, A., and Wendland, E. C.: Land use and climate change impacts on runoff and soil erosion at the hillslope scale in the Brazilian Cerrado, Sci. Total Environ., 622–623, 140–151, https://doi.org/10.1016/j.scitotenv.2017.11.257, 2018.

Angulo-Martínez, M., Beguería, S., Navas, A., and Machín, J.: Splash erosion under natural rainfall on three soil types in NE Spain, 175–176, 38–44, https://doi.org/10.1016/j.geomorph.2012.06.016, 2012.

Appels, W. M., Bogaart, P. W., and van der Zee, S. E. A. T. M.: Influence of spatial variations of microtopography and infiltration on surface runoff and field scale hydrological connectivity, Adv. Water Resour., 34, 303–313, https://doi.org/10.1016/j.advwatres.2010.12.003, 2011.

Appels, W. M., Bogaart, P. W., and van der Zee, S. E. A. T. M.: Surface runoff in flat terrain: How field topography and runoff generating processes control hydrological connectivity, J. Hydrol., 534, 493–504, https://doi.org/10.1016/j.jhydrol.2016.01.021, 2016.

Asadi, H., Shahedi, K., Jarihani, B., and Sidle, R.: Rainfall-Runoff Modelling Using Hydrological Connectivity Index and Artificial Neural Network Approach, 11, 212, https://doi.org/10.3390/w11020212, 2019.

Badr, A. A. and Lotfy, M. F.: Tracing beach sand movement using fluorescent quartz along the Nile delta promontories, Egypt, J. Coast. Res., 15, 261–265, 1999.

Bast, A., Wilcke, W., Graf, F., Lüscher, P., and Gärtner, H.: A simplified and rapid technique to determine an aggregate stability coefficient in coarse grained soils, 127, 170–176, https://doi.org/10.1016/j.catena.2014.11.017, 2015.

Bertuzzi, P., Rauws, G., and Courault, D.: Testing roughness indices to estimate soil surface roughness changes due to simulated rainfall, Soil Tillage Res., 17, 87–99, https://doi.org/https://doi.org/10.1016/0167-1987(90)90008-2, 1990.

Blanchard, D. C.: Raindrop size-distribution in Hawaiian rains, J. Meteorol., 10, 457–473, https://doi.org/10.1175/1520-0469(1953)010<0457:RSDIHR>2.0.CO;2, 1953.

Bracken, L. J. and Croke, J.: The concept of hydrological connectivity and its contribution to understanding runoff-dominated geomorphic systems, Hydrol. Process., 21, 1749–1763, https://doi.org/10.1002/hyp.6313, 2007.

Bracken, L. J., Wainwright, J., Ali, G. A., Tetzlaff, D., Smith, M. W., Reaney, S. M., and Roy, A. G.: Concepts of hydrological connectivity: Research approaches, pathways and future agendas, Earth-Science Rev., 119, 17–34, https://doi.org/10.1016/j.earscirev.2013.02.001, 2013.

Brardinoni, F. and Hassan, M. A.: Glacial erosion, evolution of river long profiles, and the organization of process domains in mountain drainage basins of coastal British Columbia, J. Geophys. Res., 111, F01013, https://doi.org/10.1029/2005JF000358, 2006.

Buda, A. R., Kleinman, P. J. A., Srinivasan, M. S., Bryant, R. B., and Feyereisen, G. W.: Factors influencing surface runoff generation from two agricultural hillslopes in central Pennsylvania, Hydrol. Process., 23, 1295–1312,

https://doi.org/10.5194/egusphere-2022-165
Preprint. Discussion started: 21 April 2022


https://doi.org/10.1002/hyp.7237, 2009.

Buendia, C., Vericat, D., Batalla, R. J., and Gibbins, C. N.: Temporal Dynamics of Sediment Transport and Transient In-channel Storage in a Highly Erodible Catchment, L. Degrad. Dev., 27, 1045–1063, https://doi.org/10.1002/ldr.2348, 2016.

Cammeraat, L. H.: A review of two strongly contrasting geomorphological systems within the context of scale, Earth Surf. Process. Landforms, 27, 1201–1222, https://doi.org/10.1002/esp.421, 2002.

Carnahan, E., Amundson, J. M., and Hood, E.: Impact of glacier loss and vegetation succession on annual basin runoff, Hydrol. Earth Syst. Sci., 23, 1667–1681, https://doi.org/10.5194/hess-23-1667-2019, 2019.

Coles, A. E. and McDonnell, J. J.: Fill and spill drives runoff connectivity over frozen ground, J. Hydrol., 558, 115–128, https://doi.org/10.1016/j.jhydrol.2018.01.016, 2018.

Cowie, N. M., Moore, R. D., and Hassan, M. A.: Effects of glacial retreat on proglacial streams and riparian zones in the Coast and North Cascade Mountains, Earth Surf. Process. Landforms, 39, 351–365, https://doi.org/10.1002/esp.3453, 2014.

Darboux, F. and Huang, C.: Does Soil Surface Roughness Increase or Decrease Water and Particle Transfers?, Soil Sci. Soc. Am. J., 69, 748–756, https://doi.org/10.2136/sssaj2003.0311, 2005.

Deasy, C. and Quinton, J. N.: Use of rare earth oxides as tracers to identify sediment source areas for agricultural hillslopes, 1, 111–118, https://doi.org/10.5194/se-1-111-2010, 2010.

Ding, W. and Li, M.: Effects of grass coverage and distribution patterns on erosion and overland flow hydraulic characteristics, Environ. Earth Sci., 75, 477, https://doi.org/10.1007/s12665-016-5329-7, 2016.

Dunkerley, D.: Flow threads in surface run-off: implications for the assessment of flow properties and friction coefficients in soil erosion and hydraulics investigations, Earth Surf. Process. Landforms, 29, 1011–1026, https://doi.org/10.1002/esp.1086, 2004.

Dunkerley, D. L.: Determining friction coefficients for interrill flows: the significance of flow filaments and backwater effects, Earth Surf. Process. Landforms, 28, 475–491, https://doi.org/10.1002/esp.453, 2003.

Dunne, T., Zhang, W., and Aubry, B. F.: Effects of Rainfall, Vegetation, and Microtopography on Infiltration and Runoff, Water Resour. Res., 27, 2271–2285, https://doi.org/10.1029/91WR01585, 1991.

Ebabu, K., Tsunekawa, A., Haregeweyn, N., Adgo, E., Meshesha, D. T., Aklog, D., Masunaga, T., Tsubo, M., Sultan, D., Fenta, A. A., and Yibeltal, M.: Analyzing the variability of sediment yield: A case study from paired watersheds in the Upper Blue Nile basin, Ethiopia, 303, 446–455, https://doi.org/10.1016/j.geomorph.2017.12.020, 2018.

Eigel, J. and Moore, I. D.: A simplified technique for measuring raindrop size and distribution, Trans. ASAE, 26, 1079–1084, 1983.

Evans, R.: Mechanics of ater erosion and their spatial and temporal controls: an empirical viewpoint., Soil Erosion. Wiley, Chichester, 109–128, 1980.

Farmer, E. E.: Soil erosion by overland flow and raindrop splash on three mountain soils, (No. 92-10., Intermountain Forest & Range Experiment Station, Forest Service, US Department of Agriculture., 1971.

Fernández-Raga, M., Palencia, C., Keesstra, S., Jordán, A., Fraile, R., Angulo-Martínez, M., and Cerdà, A.: Splash erosion: A review with unanswered questions, Earth-Science Rev., 171, 463–477, https://doi.org/10.1016/j.earscirev.2017.06.009, 2017.

Garnier, E., Navas, M. L., and Grigulis, K.: Plant functional diversity: organism traits, community structure, and ecosystem properties, Oxford University Press, 2016.

Gay, A., Cerdan, O., Mardhel, V., and Desmet, M.: Application of an index of sediment connectivity in a lowland area, J. Soils Sediments, 16, 280–293, https://doi.org/10.1007/s11368-015-1235-y, 2016.

Geilhausen, M., Morche, D., Otto, J.-C., and Schrott, L.: Sediment discharge from the proglacial zone of a retreating Alpine glacier, Zeitschrift für Geomorphol. Suppl. Issues, 57, 29–53, https://doi.org/10.1127/0372-8854/2012/S-00122, 2013.

https://doi.org/10.5194/egusphere-2022-165
Preprint. Discussion started: 21 April 2022


Geißler, C., Lang, A. C., von Oheimb, G., Härdtle, W., Baruffol, M., and Scholten, T.: Impact of tree saplings on the kinetic energy of rainfall—The importance of stand density, species identity and tree architecture in subtropical forests in China, Agric. For. Meteorol., 156, 31–40, https://doi.org/10.1016/j.agrformet.2011.12.005, 2012.

Gerke, K. M., Sidle, R. C., and Mallants, D.: Preferential flow mechanisms identified from staining experiments in forested hillslopes, Hydrol. Process., 29, 4562–4578, https://doi.org/10.1002/hyp.10468, 2015.

Gianinetto, M., Aiello, M., Vezzoli, R., Polinelli, F. N., Rulli, M. C., Chiarelli, D. D., Bocchiola, D., Ravazzani, G., and Soncini, A.: Future Scenarios of Soil Erosion in the Alps under Climate Change and Land Cover Transformations Simulated with Automatic Machine Learning, 8, 28, https://doi.org/10.3390/cli8020028, 2020.

van De Giesen, N. C., Stomph, T. J., and de Ridder, N.: Scale effects of Hortonian overland flow and rainfall-runoff dynamics in a West African catena landscape, Hydrol. Process., 14, 165–175, https://doi.org/10.1002/(SICI)1099-1085(200001)14:1<165::AID-HYP920>3.0.CO;2-1, 2000.

Gomi, T., Sidle, R. C., Miyata, S., Kosugi, K., and Onda, Y.: Dynamic runoff connectivity of overland flow on steep forested hillslopes: Scale effects and runoff transfer, Water Resour. Res., 44, 1–16, https://doi.org/10.1029/2007WR005894, 2008.

Govers, G., Takken, I., and Helming, K.: Soil roughness and overland flow, 20, 131–146, https://doi.org/10.1051/agro:2000114, 2000.

Greinwald, K., Gebauer, T., Treuter, L., Kolodziej, V., Musso, A., Maier, F., Lustenberger, F., and Scherer-Lorenzen, M.: Root density drives aggregate stability of soils of different moraine ages in the Swiss Alps, Plant Soil, https://doi.org/10.1007/s11104-021-05111-8, 2021a.

Greinwald, K., Dieckmann, L. A., Schipplick, C., Hartmann, A., Scherer-Lorenzen, M., and Gebauer, T.: Vertical root distribution and biomass allocation along proglacial chronosequences in Central Switzerland, Arctic, Antarct. Alp. Res., 53, 20–34, https://doi.org/10.1080/15230430.2020.1859720, 2021b.

Guzmán, G., Barrón, V., and Gómez, J. A.: Evaluation of magnetic iron oxides as sediment tracers in water erosion experiments, 82, 126–133, https://doi.org/10.1016/j.catena.2010.05.011, 2010.

Guzmán, G., Laguna, A., Cañasveras, J. C., Boulal, H., Barrón, V., Gómez-Macpherson, H., Giráldez, J. V., and Gómez, J. A.: Study of sediment movement in an irrigated maize–cotton system combining rainfall simulations, sediment tracers and soil erosion models, J. Hydrol., 524, 227–242, https://doi.org/10.1016/j.jhydrol.2015.02.033, 2015.

Gyssels, G., Poesen, J., Bochet, E., and Li, Y.: Impact of plant roots on the resistance of soils to erosion by water: a review, Prog. Phys. Geogr. Earth Environ., 29, 189–217, https://doi.org/10.1191/0309133305pp443ra, 2005.

Hachani, S., Boudevillain, B., Delrieu, G., and Bargaoui, Z.: Drop size distribution climatology in Cévennes-Vivarais region, France, Atmosphere (Basel)., 8, https://doi.org/10.3390/atmos8120233, 2017.

Harden, C. P. and Scruggs, P. D.: Infiltration on mountain slopes: a comparison of three environments, 55, 5–24, https://doi.org/10.1016/S0169-555X(03)00129-6, 2003.

Hardy, R. A., Pates, J. M., Quinton, J. N., and Coogan, M. P.: A novel fluorescent tracer for real-time tracing of clay transport over soil surfaces, 141, 39–45, https://doi.org/10.1016/j.catena.2016.02.011, 2016.

Hardy, R. A., James, M. R., Pates, J. M., and Quinton, J. N.: Using real time particle tracking to understand soil particle movements during rainfall events, 150, 32–38, https://doi.org/10.1016/j.catena.2016.11.005, 2017.

Hardy, R. A., Quinton, J. N., James, M. R., Fiener, P., and Pates, J. M.: High precision tracing of soil and sediment movement using fluorescent tracers at hillslope scale, Earth Surf. Process. Landforms, 44, 1091–1099, https://doi.org/10.1002/esp.4557, 2019.

Hartmann, A., Semenova, E., Weiler, M., and Blume, T.: Field observations of soil hydrological flow path evolution over 10 Millennia, Hydrol. Earth Syst. Sci., 28, 1–26, https://doi.org/10.5194/hess-2020-28, 2020a.

Hartmann, A., Weiler, M., and Blume, T.: The impact of landscape evolution on soil physics: Evolution of soil physical and hydraulic properties along two chronosequences of proglacial moraines, Earth Syst. Sci. Data, 1–26,

https://doi.org/10.5194/essd-2020-110, 2020b.

Heckmann, T. and Schwanghart, W.: Geomorphic coupling and sediment connectivity in an alpine catchment — Exploring sediment cascades using graph theory, 182, 89–103, https://doi.org/10.1016/j.geomorph.2012.10.033, 2013.

Heckmann, T., Cavalli, M., Cerdan, O., Foerster, S., Javaux, M., Lode, E., Smetanová, A., Vericat, D., and Brardinoni, F.: Indices of sediment connectivity: opportunities, challenges and limitations, Earth-Science Rev., 187, 77–108, https://doi.org/10.1016/j.earscirev.2018.08.004, 2018.

Helming, K., Römkens, M. J. M., and Prasad, S. N.: Surface Roughness Related Processes of Runoff and Soil Loss: A Flume Study, Soil Sci. Soc. Am. J., 62, 243–250, https://doi.org/10.2136/sssaj1998.03615995006200010031x, 1998.

Hino, M., Fujita, K., and Shutto, H.: A laboratory experiment on the role of grass for infiltration and runoff processes, J. Hydrol., 90, 303–325, https://doi.org/10.1016/0022-1694(87)90073-4, 1987.

Hock, R., Rasul, G., Adler, C., Cáceres, B., Gruber, S., Hirabayashi, Y., Jackson, M., Kääb, A., Kang, S., Kutuzov, S., Milner, A., Molau, U., Morin, S., Orlove, B., and Steltzer, H. I.: Chapter 2: High Mountain Areas., IPCC Spec. Rep. Ocean Cryosph. a Chang. Clim., 131–202, 2019.

Hoegh-Guldberg, O., Jacob, D., Bindi, M., Brown, S., Camilloni, I., Diedhiou, A., Djalante, R., Ebi, K., Engelbrecht, F., Guiot, J., and Hijioka, Y.: Impacts of 1.5°C global warming on natural and human systems. In: Global Warming of 1.5 °C. An IPCC Special Report, Special Report, Intergovernmental Panel on Climate Change, 175–311 pp., 2018.

Horton, R. E.: The role of infiltration in the hydrologic cycle, Eos, Trans. Am. Geophys. Unioneophysical Union, 14, 446–460, 1933.

Hudek, Sturrock, C. J., Atkinson, B. S., Stanchi, S., and Freppaz, M.: Root morphology and biomechanical characteristics of high altitude alpine plant species and their potential application in soil stabilization, Ecol. Eng., 109, 228–239, https://doi.org/10.1016/j.ecoleng.2017.05.048, 2017.

Ingle, J. C.: The Movement of Beach Sand - An Analysis Using Fluorescent Grains, 1st ed., Elsevier, https://doi.org/10.1016/S0070-4571(08)X7030-X, 1966.

Johnson, C. B., Mannering, J. V., and Moldenhauer, W. C.: Influence of Surface Roughness and Clod Size and Stability on Soil and Water Losses, Soil Sci. Soc. Am. J., 43, 772–777, https://doi.org/10.2136/sssaj1979.03615995004300040031x, 1979.

Jomaa, S., Barry, D. A., Heng, B. C. P., Brovelli, A., Sander, G. C., and Parlange, J.-Y.: Influence of rock fragment coverage on soil erosion and hydrological response: Laboratory flume experiments and modeling, Water Resour. Res., 48, https://doi.org/10.1029/2011WR011255, 2012.

Jonasson, S. and Callaghan, T. V: Root mechanical properties related to disturbed and stressed habitats in the Arctic, New Phytol., 122, 179–186, https://doi.org/10.1111/j.1469-8137.1992.tb00064.x, 1992.

Kato, S., Okabe, T., Aoki, Y., and Kamohara, S.: Field measurements of sand movement on river-mouth tidal flat using color sand tracing, Coast. Eng. Proc., 1, 61, https://doi.org/10.9753/icce.v34.sediment.61, 2014.

Klaar, M. J., Kidd, C., Malone, E., Bartlett, R., Pinay, G., Chapin, F. S., and Milner, A.: Vegetation succession in deglaciated landscapes: implications for sediment and landscape stability, Earth Surf. Process. Landforms, 40, 1088–1100, https://doi.org/10.1002/esp.3691, 2015.

Klein, M., Zviely, D., Kit, E., and Shteinman, B.: Sediment Transport along the Coast of Israel: Examination of Fluorescent Sand Tracers, J. Coast. Res., 236, 1462–1470, https://doi.org/10.2112/05-0488.1, 2007.

Knapen, A., Poesen, J., Govers, G., Gyssels, G., and Nachtergaele, J.: Resistance of soils to concentrated flow erosion: A review, Earth-Science Rev., 80, 75–109, https://doi.org/10.1016/j.earscirev.2006.08.001, 2007.

Komura, S.: Hydraulics of Slope Erosion by Overland Flow, J. Hydraul. Div., 102, 1573–1586, https://doi.org/10.1061/JYCEAJ.0004639, 1976.

Labhart, T. P.: Aarmassiv und Gotthardmassiv, Sammlung Geol. Führer, 63, 173, 1977.

https://doi.org/10.5194/egusphere-2022-165
Preprint. Discussion started: 21 April 2022


Lane, S. N., Reaney, S. M., and Heathwaite, A. L.: Representation of landscape hydrological connectivity using a topographically driven surface flow index, Water Resour. Res., 45, 1–10, https://doi.org/10.1029/2008WR007336, 2009.

Lavee, H. and Poesen, J. W. A.: Overland flow generation and continuity on stone-covered soil surfaces, Hydrol. Process., 5, 345–360, https://doi.org/10.1002/hyp.3360050403, 1991.

Lázaro, R., Calvo-Cases, A., Lázaro, A., and Molina, I.: Effective run-off flow length over biological soil crusts on silty loam soils in drylands, Hydrol. Process., 29, 2534–2544, https://doi.org/10.1002/hyp.10345, 2015.

Leatherman, S. P.: Field Measurement of Microtopography, J. Coast. Res., 3, 233–235, 1987.

Legout, C., Leguédois, S., Le Bissonnais, Y., and Malam Issa, O.: Splash distance and size distributions for various soils, Geoderma, 124, 279–292, https://doi.org/10.1016/j.geoderma.2004.05.006, 2005.

Lichtenegger, E.: Root distribution in some alpine plants, Acta Phytogeogr. Suec., 81, 76–82, 1996.

Lima, R. L. P. de, Abrantes, J. R. C. B., Lima, J. L. M. P. de, and Lima, M. I. P. de: Using thermal tracers to estimate flow velocities of shallow flows: laboratory and field experiments, J. Hydrol. Hydromechanics, 63, 255–262, https://doi.org/10.1515/johh-2015-0028, 2015.

Liu, Q. Q. and Singh, V. P.: Effect of Microtopography, Slope Length and Gradient, and Vegetative Cover on Overland Flow through Simulation, J. Hydrol. Eng., 9, 375–382, https://doi.org/10.1061/(ASCE)1084-0699(2004)9:5(375), 2004.

Lohse, K. A. and Dietrich, W. E.: Contrasting effects of soil development on hydrological properties and flow paths, Water Resour. Res., 41, 1–17, https://doi.org/10.1029/2004WR003403, 2005.

Maier, F. and van Meerveld, I.: Long-Term Changes in Runoff Generation Mechanisms for Two Proglacial Areas in the Swiss Alps I: Overland Flow, Water Resour. Res., 57, 1–30, https://doi.org/10.1029/2021wr030221, 2021.

Maier, F., van Meerveld, I., Greinwald, K., Gebauer, T., Lustenberger, F., Hartmann, A., and Musso, A.: Effects of soil and vegetation development on surface hydrological properties of moraines in the Swiss Alps, 187, 104353, https://doi.org/10.1016/j.catena.2019.104353, 2020.

Marques, M. J., Bienes, R., Jiménez, L., and Pérez-Rodríguez, R.: Effect of vegetal cover on runoff and soil erosion under light intensity events. Rainfall simulation over USLE plots, Sci. Total Environ., 378, 161–165, https://doi.org/10.1016/j.scitotenv.2007.01.043, 2007.

Masselink, R. J. H., Heckmann, T., Temme, A. J. A. M., Anders, N. S., Gooren, H. P. A., and Keesstra, S. D.: A network theory approach for a better understanding of overland flow connectivity, Hydrol. Process., 31, 207–220, https://doi.org/10.1002/hyp.10993, 2017.

Medeiros, P. H. A. and de Araújo, J. C.: Temporal variability of rainfall in a semiarid environment in Brazil and its effect on sediment transport processes, J. Soils Sediments, 14, 1216–1223, https://doi.org/10.1007/s11368-013-0809-9, 2013.

MeteoSwiss. Swiss climate in detail. Extreme value analysis. Standard period 1990-2020. URL: https://www.meteoschweiz.admin.ch/home/klima/schweizer-klima-im-detail/extremwertanalysen/standardperiode.html?station=grh (last date accessed: 17.02.2022), 2021.

MeteoSwiss. Swiss climate in detail. Climate diagrams and normals per station. Standard period 1991-2020. URL: https://www.meteoschweiz.admin.ch/home/klima/schweizer-klima-im-detail/klima-normwerte/klimadiagramme-und-normwerte-pro-station.html?station=grh (last date accessed: 17.02.2022), 2022.

Moreno-De Las Heras, M., Nicolau, J. M., Merino-Martn, L., and Wilcox, B. P.: Plot-scale effects on runoff and erosion along a slope degradation gradient, Water Resour. Res., 46, 1–12, https://doi.org/10.1029/2009WR007875, 2010.

Mu, H., Yu, X., Fu, S., Yu, B., Liu, Y., and Zhang, G.: Effect of stem basal cover on the sediment transport capacity of overland flows, Geoderma, 337, 384–393, https://doi.org/10.1016/j.geoderma.2018.09.055, 2019.

Musso, A., Lamorski, K., Sławiński, C., Geitner, C., Hunt, A., Greinwald, K., and Egli, M.: Evolution of soil pores and their characteristics in a siliceous and calcareous proglacial area, 182, 104–154, https://doi.org/10.1016/j.catena.2019.104154, 2019.

https://doi.org/10.5194/egusphere-2022-165
Preprint. Discussion started: 21 April 2022


Musso, A., Ketterer, M. E., Greinwald, K., Geitner, C., and Egli, M.: Rapid decrease of soil erosion rates with soil formation and vegetation development in periglacial areas, Earth Surf. Process. Landforms, 45, 2824–2839, https://doi.org/10.1002/esp.4932, 2020a.

Musso, A., Ketterer, M. E., Greinwald, K., Geitner, C., and Egli, M.: Rapid decrease of soil erosion rates with soil formation and vegetation development in periglacial areas, Earth Surf. Process. Landforms, 45, 2824–2839, https://doi.org/10.1002/esp.4932, 2020b.

Najafi, S., Dragovich, D., Heckmann, T., and Sadeghi, S. H.: Sediment connectivity concepts and approaches, 196, 104880, https://doi.org/10.1016/j.catena.2020.104880, 2021.

Nanda, A., Sen, S., and McNamara, J. P.: How spatiotemporal variation of soil moisture can explain hydrological connectivity of infiltration-excess dominated hillslope: Observations from lesser Himalayan landscape, J. Hydrol., 579, 124146, https://doi.org/10.1016/j.jhydrol.2019.124146, 2019.

Nearing, M. A., Pruski, F. ., and O'Neal, M. R.: Expected climate change impacts on soil erosion rates: A review, J. Soil Water Conserv. Soc., 59, 43–50, 2004.

Material safety data sheet of glow in the dark powder TAT 33: http://noxton.net/pasport_en.html (website last accessed: 26.02.2022).

Orwin, J. F., Guggenmos, M. R., and Holland, P. G.: Changes in suspended sediment to solute yield ratios from an alpine basin during the transition to winter, southern alps, New zealand, Geogr. Ann. Ser. A Phys. Geogr., 92, 247–261, https://doi.org/10.1111/j.1468-0459.2010.00393.x, 2010.

Panagos, P., Borrelli, P., Poesen, J., Ballabio, C., Lugato, E., Meusburger, K., Montanarella, L., and Alewell, C.: The new assessment of soil loss by water erosion in Europe, Environ. Sci. Policy, 54, 438–447, https://doi.org/10.1016/j.envsci.2015.08.012, 2015.

Park, S. W., Mitchell, J. K., and Bubenzern, G. D.: Rainfall Characteristics and Their Relation to Splash Erosion, Trans. ASAE, 26, 0795–0804, https://doi.org/10.13031/2013.34026, 1983.

Parsons, A. J.: Overland Flow. Hydraulics and Erosion Mechanics., 1st ed., edited by: Parsons, A. J., CRC Press, London, 456 pp., https://doi.org/10.1201/b12648, 1992.

Parsons, A. J.: Erosion and Sediment Transport by Water on Hillslopes, in: Encyclopedia of Water, Wiley, 1–10, https://doi.org/10.1002/9781119300762.wsts0007, 2019.

Parsons, A. J., Onda, Y., Noguchi, T., Patin, J., Cooper, J., Wainwright, J., and Sakai, N.: The use of RFID in soil-erosion research, Earth Surf. Process. Landforms, 39, 1693–1696, https://doi.org/10.1002/esp.3628, 2014.

Paschmann, C., Fernandes, J. N., Vetsch, D. F., and Boes, R. M.: Assessment of flow field and sediment flux at alpine desanding facilities, Int. J. River Basin Manag., 15, 287–295, https://doi.org/10.1080/15715124.2017.1280814, 2017.

Pearce, R. A., Trlica, M. J., Leininger, W. C., Smith, J. L., and Frasier, G. W.: Efficiency of Grass Buffer Strips and Vegetation Height on Sediment Filtration in Laboratory Rainfall Simulations, J. Environ. Qual., 26, 139–144, https://doi.org/10.2134/jeq1997.00472425002600010021x, 1997.

Peñuela, A., Darboux, F., Javaux, M., and Bielders, C. L.: Evolution of overland flow connectivity in bare agricultural plots, Earth Surf. Process. Landforms, 41, 1595–1613, https://doi.org/10.1002/esp.3938, 2016.

Poesen, J.: Soil erosion in the Anthropocene: Research needs, Earth Surf. Process. Landforms, 84, 64–84, https://doi.org/10.1002/esp.4250, 2017.

Poesen, J. and Lavee, H.: Rock fragments in top soils: significance and processes, 23, 1–28, https://doi.org/10.1016/0341-8162(94)90050-7, 1994.

Poesen, J., Ingelmo-Sanchez, F., and Mucher, H.: The hydrological response of soil surfaces to rainfall as affected by cover and position of rock fragments in the top layer, Earth Surf. Process. Landforms, 15, 653–671, https://doi.org/10.1002/esp.3290150707, 1990.

https://doi.org/10.5194/egusphere-2022-165
Preprint. Discussion started: 21 April 2022


Pohl, M., Stroude, R., Buttler, A., and Rixen, C.: Functional traits and root morphology of alpine plants, Ann. Bot., 108, 537–545, https://doi.org/10.1093/aob/mcr169, 2011.

Polyakov, V., Li, L., and Nearing, M. A.: Correction factor for measuring mean overland flow velocities on stony surfaces under rainfall using dye tracer, Geoderma, 390, 114975, https://doi.org/10.1016/j.geoderma.2021.114975, 2021.

Polyakov, V. . and Nearing, M. .: Rare earth element oxides for tracing sediment movement, 55, 255–276, https://doi.org/10.1016/S0341-8162(03)00159-0, 2004.

Raclot, D., Le Bissonnais, Y., Annabi, M., Sabir, M., and Smetanova, A.: Main Issues for Preserving Mediterranean Soil Resources From Water Erosion Under Global Change, L. Degrad. Dev., 29, 789–799, https://doi.org/10.1002/ldr.2774, 2018.

Reaney, S. M., Bracken, L. J., and Kirkby, M. J.: The importance of surface controls on overland flow connectivity in semi-arid environments: results from a numerical experimental approach, Hydrol. Process., 28, 2116–2128, https://doi.org/10.1002/hyp.9769, 2014.

Rey, F.: Influence of vegetation distribution on sediment yield in forested marly gullies, 50, 549–562, https://doi.org/10.1016/S0341-8162(02)00121-2, 2003.

Rey, F., Ballais, J.-L., Marre, A., and Rovéra, G.: Role of vegetation in protection against surface hydric erosion, Comptes Rendus Geosci., 336, 991–998, https://doi.org/10.1016/j.crte.2004.03.012, 2004.

Richards, J. A.: Supervised Classification Techniques, in: Remote Sensing Digital Image Analysis, Springer Berlin Heidelberg, Berlin, Heidelberg, 247–318, https://doi.org/10.1007/978-3-642-30062-2_8, 2013.

Schneider, P., Pool, S., Strouhal, L., and Seibert, J.: True colors – experimental identification of hydrological processes at a hillslope prone to slide, Hydrol. Earth Syst. Sci., 18, 875–892, https://doi.org/10.5194/hess-18-875-2014, 2014.

Sen, S., Srivastava, P., Dane, J. H., Yoo, K. H., and Shaw, J. N.: Spatial-temporal variability and hydrologic connectivity of runoff generation areas in a North Alabama pasture-implications for phosphorus transport, Hydrol. Process., 24, 342–356, https://doi.org/10.1002/hyp.7502, 2010.

Shore, M., Murphy, P. N. C., Jordan, P., Mellander, P.-E., Kelly-Quinn, M., Cushen, M., Mechan, S., Shine, O., and Melland, A. R.: Evaluation of a surface hydrological connectivity index in agricultural catchments, Environ. Model. Softw., 47, 7–15, https://doi.org/10.1016/j.envsoft.2013.04.003, 2013.

Sidle, R. C., Hirano, T., Gomi, T., and Tomomi, T.: Hortonian overland flow from Japanese forest plantations — an aberration, the real thing, or something in between ?, Hydrol. Process., 21, 3237–3247, https://doi.org/10.1002/hyp, 2007.

Singer, M. and Walker, P.: Rainfall runoff in soil erosion with simulated rainfall, overland flow and cover, Soil Res., 21, 109, https://doi.org/10.1071/SR9830109, 1983.

Smith, M. W., Bracken, L. J., and Cox, N. J.: Toward a dynamic representation of hydrological connectivity at the hillslope scale in semiarid areas, Water Resour. Res., 46, 1–18, https://doi.org/10.1029/2009WR008496, 2010.

Stewart, R. D., Liu, Z., Rupp, D. E., Higgins, C. W., and Selker, J. S.: A new instrument to measure plot-scale runoff, Geosci. Instrumentation, Methods Data Syst., 4, 57–64, https://doi.org/10.5194/gi-4-57-2015, 2015.

Stock, J. and Dietrich, W. E.: Valley incision by debris flows: Evidence of a topographic signature, Water Resour. Res., 39, https://doi.org/10.1029/2001WR001057, 2003.

Stoffel, M., Mendlik, T., Schneuwly-Bollschweiler, M., and Gobiet, A.: Possible impacts of climate change on debris-flow activity in the Swiss Alps, Clim. Change, 122, 141–155, https://doi.org/10.1007/s10584-013-0993-z, 2014.

Tarboton, D. G.: A new method for the determination of flow directions and upslope areas in grid digital elevation models, Water Resour. Res., 33, 309–319, https://doi.org/10.1029/96WR03137, 1997.

Tauro, F., Grimaldi, S., Petroselli, A., and Porfiri, M.: Fluorescent particle tracers for surface flow measurements: A proof of concept in a natural stream, Water Resour. Res., 48, https://doi.org/10.1029/2011WR011610, 2012a.

Tauro, F., Grimaldi, S., Petroselli, A., Rulli, M. C., and Porfiri, M.: Fluorescent particle tracers in surface hydrology: a proof

https://doi.org/10.5194/egusphere-2022-165
Preprint. Discussion started: 21 April 2022


of concept in a semi-natural hillslope, Hydrol. Earth Syst. Sci., 16, 2973–2983, https://doi.org/10.5194/hess-16-2973-2012, 2012b.

Tauro, F., Petroselli, A., Fiori, A., Romano, N., Rulli, M. C., Porfiri, M., Palladino, M., and Grimaldi, S.: Technical Note: Monitoring streamflow generation processes at Cape Fear, Hydrol. Earth Syst. Sci. Discuss., 1–25, https://doi.org/10.5194/hess-2016-501, 2016.

Thompson, S. E., Katul, G. G., and Porporato, A.: Role of microtopography in rainfall-runoff partitioning: An analysis using idealized geometry, Water Resour. Res., 46, 1–11, https://doi.org/10.1029/2009WR008835, 2010a.

Thompson, S. E., Harman, C. J., Heine, P., and Katul, G. G.: Vegetation-infiltration relationships across climatic and soil type gradients, J. Geophys. Res. Biogeosciences, 115, n/a-n/a, https://doi.org/10.1029/2009JG001134, 2010b.

Vigiak, O., van Dijck, S. J. E., van Loon, E. E., and Stroosnijder, L.: Matching hydrologic response to measured effective hydraulic conductivity, Hydrol. Process., 20, 487–504, https://doi.org/10.1002/hyp.5916, 2006.

Wainwright, J., Parsons, A. J., and Abrahams, A. D.: Plot-scale studies of vegetation, overland flow and erosion interactions: case studies from Arizona and New Mexico, Hydrol. Process., 14, 2921–2943, https://doi.org/10.1002/1099-1085(200011/12)14:16/17<2921::AID-HYP127>3.0.CO;2-7, 2000.

Weiler, M.: Mechanisms controlling macropore flow during infiltration: dye tracer experiments and simulations, ETH Zurich, 12–19 pp., 2001.

Weiler, M. and Flühler, H.: Inferring flow types from dye patterns in macroporous soils, Geoderma, 120, 137–153, https://doi.org/10.1016/j.geoderma.2003.08.014, 2004.

Wolstenholme, J. M., Smith, M. W., Baird, A. J., and Sim, T. G.: A new approach for measuring surface hydrological connectivity, Hydrol. Process., 34, 538–552, https://doi.org/10.1002/hyp.13602, 2020.

Yasso, W. E.: Formulation and use of fluorescent tracer coatings in sediment transport studies, Sedimentology, 6, 287–301, https://doi.org/10.1111/j.1365-3091.1966.tb01896.x, 1966.

Young, R. A. and Holt, R. F.: Tracing Soil Movement with Fluorescent Glass Particles, Soil Sci. Soc. Am. J., 32, 600–602, https://doi.org/10.2136/sssaj1968.03615995003200040050x, 1968.

Zanandrea, F., Michel, G. P., Kobiyama, M., Censi, G., and Abatti, B. H.: Spatial-temporal assessment of water and sediment connectivity through a modified connectivity index in a subtropical mountainous catchment, 204, 105380, https://doi.org/10.1016/j.catena.2021.105380, 2021.

Zhang, B., Yang, Y., and Zepp, H.: Effect of vegetation restoration on soil and water erosion and nutrient losses of a severely eroded clayey Plinthudult in southeastern China, 57, 77–90, https://doi.org/10.1016/j.catena.2003.07.001, 2004.

Zimmermann, B.: Spatial and temporal variability of soil saturated hydraulic conductivity in gradients of disturbance, J. Hydrol., 361, 78–95, https://doi.org/10.1016/j.jhydrol.2008.07.027, 2008.

https://doi.org/10.5194/egusphere-2022-165
Preprint. Discussion started: 21 April 2022


Table 1: Overview of the main characteristics (elevation, slope, aspect, dominant species, vegetation cover, rock cover, sand content of the upper 10 cm of the soil, and the tortuosity index) for the five study plots.

| moraine | plot name | veg. complexity | elevation (m a.s.l.) | slope (°) | aspect (°) | dominant vegetation | veg. cover (%) | rock cover (%) | sand content (%)[1] | tortuosity index (-)[2] |
|---|---|---|---|---|---|---|---|---|---|---|
| 1860 | 1860L | low | 1989 | 28 | 49 NE | Anthoxanthum alpinum, Salix retusa | 80 | 3 | 89 | 0.29 |
| | 1860M | medium | 1981 | 36 | 56 NE | Campanula scheuchzeri, Trifolium pallescens | 80 | 2 | 65 | 0.29 |
| 1990 | 1990L | low | 1952 | 21 | 48 NE | Salix hastata | 50 | 30 | 72 | 0.52 |
| | 1990M | medium | 1959 | 29 | 56 NE | Epilobium fleischeri, Poa alpina | 30 | 12 | 77 | 0.36 |
| | 1990H | high | 1955 | 22 | 28 NE | Salix retusa, Trifolium pallescens | 45 | 19 | 75 | 0.55 |

[1] from Hartmann et al. (2020b).
[2] calculated by the method of Bertuzzi et al. (1990), based on the normalized line length for ten measurements on each plot with a microtopography profiler of 1.5 m length (cf. Leatherman, 1987).

Table 2: Overview of the main response characteristics for all low, medium and high-intensity sprinkling experiments (LI, MI and HI, respectively) on all five plots. $P_{tot}$ is the total rainfall amount, $P_{int}$ is the average rainfall intensity, $t_P$ is the rainfall duration, $OF_{tot}$ is the total overland flow (OF), $OF_{peak}$ is the peak OF rate, $T_{peak}$ is the peak turbidity, $S_Y$ is the sediment yield, $\Delta D$ is the percent change in sand distance, and $\Delta A$ is the percent change in sand-covered area.

| moraine | plot | experiment | $P_{tot}$ (mm) | $P_{int}$ (mm hr$^{-1}$) | $t_P$ (min) | $OF_{tot}$ (mm) | $OF_{peak}$ (mm h$^{-1}$) | $T_{peak}$ (NTU) | $S_Y$ (g) | $\Delta D$ (%) | $\Delta A$ (%) |
|---|---|---|---|---|---|---|---|---|---|---|---|
| 1860 | 1860L | LI | 23 | 20 | 69 | 0 | 0 | 0 | 0 | -15 | -16 |
| | | MI | 25 | 43 | 35 | 1 | 4.9 | 11 | 1 | 31 | -19 |
| | | HI | 57 | 81 | 42 | 1.7 | 6.9 | 12 | 2 | 103 | 87 |
| | 1860M | LI | 23 | 22 | 64 | 0 | 0 | 0 | 0 | -46 | -52 |
| | | MI | 52 | 56 | 56 | 0 | 0 | 0 | 0 | 11 | -27 |
| | | HI | 63 | 90 | 42 | 1.3 | 7.2 | 2 | 0 | -3 | -38 |
| 1990 | 1990L | LI | 19 | 15 | 75 | 1.4 | 0.5 | 48 | 1 | 253 | 272 |
| | | MI | 30 | 37 | 48 | 3.1 | 8 | 83 | 28 | 334 | 198 |
| | | HI | 32 | 48 | 40 | 3.6 | 10.6 | 134 | 46 | 265 | 211 |
| | 1990M | LI | 21 | 23 | 55 | 0 | 0 | 0 | 0 | 152 | 139 |
| | | MI | 33 | 54 | 37 | 0 | 0 | 0 | 0 | 190 | 165 |
| | | HI | 36 | 61 | 35 | 2.4 | 9.2 | 39 | 4 | 175 | 160 |
| | 1990H | LI | 18 | 14 | 75 | 1.9 | 2.4 | 7 | 0 | 15 | 22 |
| | | MI | 27 | 33 | 49 | 1.6 | 3.3 | 89 | 6 | 38 | 24 |
| | | HI | 27 | 46 | 35 | 1.8 | 5.4 | 94 | 15 | 79 | 26 |

https://doi.org/10.5194/egusphere-2022-165
Preprint. Discussion started: 21 April 2022


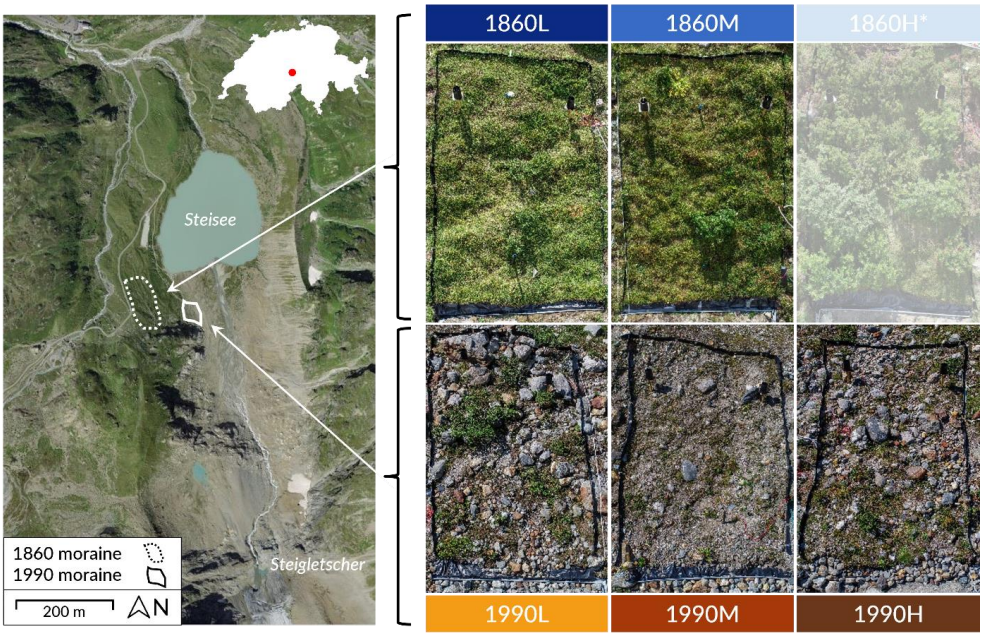


Figure 1: Aerial image of the Sustenpass study area (left) and photographs of the three experimental plots (right) on the 1860 and 1990 moraines. The aerial image of the study area shows the outlines of the two studied moraines (1860 moraine: dashed line; 1990 moraine: solid line). The vegetation cover for the older (1860) moraine (top) is much higher than for the younger (1990) moraine (bottom). The 1860H plot was excluded from the analysis due to the dense shrub cover. Source of the aerial image: Federal Office of Topography Swisstopo ('Journey through time', 2019).

https://doi.org/10.5194/egusphere-2022-165
Preprint. Discussion started: 21 April 2022


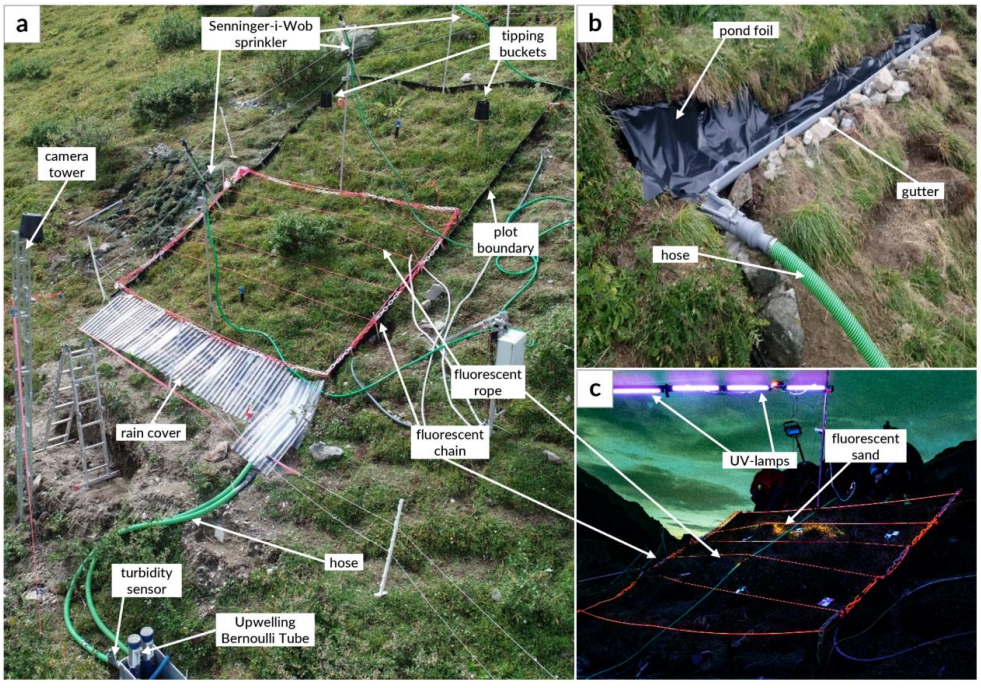


Figure 2: Photos showing the experimental set-up for all study plots (a), the collection system for overland flow (OF), biomat and very shallow subsurface flow (b), and the set-up for the fluorescent sand imaging (c). Important components, such as the plot borders, sprinklers, tipping bucket rain gauges, pond foil, gutter and hose, turbidity sensor and Upwelling Bernoulli Tube, the fluorescent segmented chain and fluorescent ropes, and camera tower below the plot are marked and labeled. At night UV lamps were used to illuminate the fluorescent sand on the plot (c).

https://doi.org/10.5194/egusphere-2022-165
Preprint. Discussion started: 21 April 2022


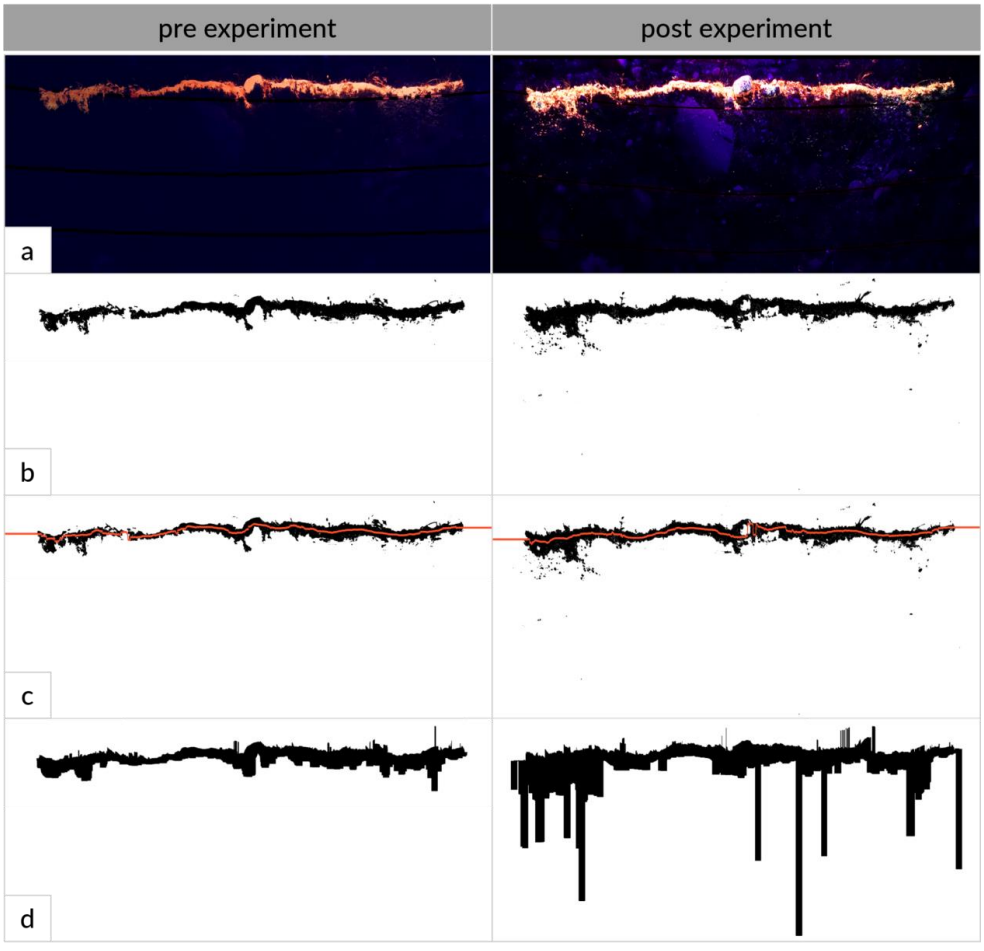


Figure 3: Pre and post sprinkling photographs (a) and visualization of the steps taken for the image analysis (b, c, d): geometrically corrected photos with the plot surroundings cut off and the fluorescent ropes digitally removed from the picture (a), classified images (a visual representation of a matrix containing zeros and ones) where classified pixels with fluorescent sand are shown in black (b), classified images with the location of the starting line (in red, at approximately the middle of the sand ribbon) for the determination of sand distances (c) and the calculated areas over which the sand was spread (d). The photos and images shown here are for the 1990M plot before and after the low intensity (LI) experiment. Please note that due to the downscaling of the photos and images not all sand particles are visible in the pictures.

https://doi.org/10.5194/egusphere-2022-165
Preprint. Discussion started: 21 April 2022


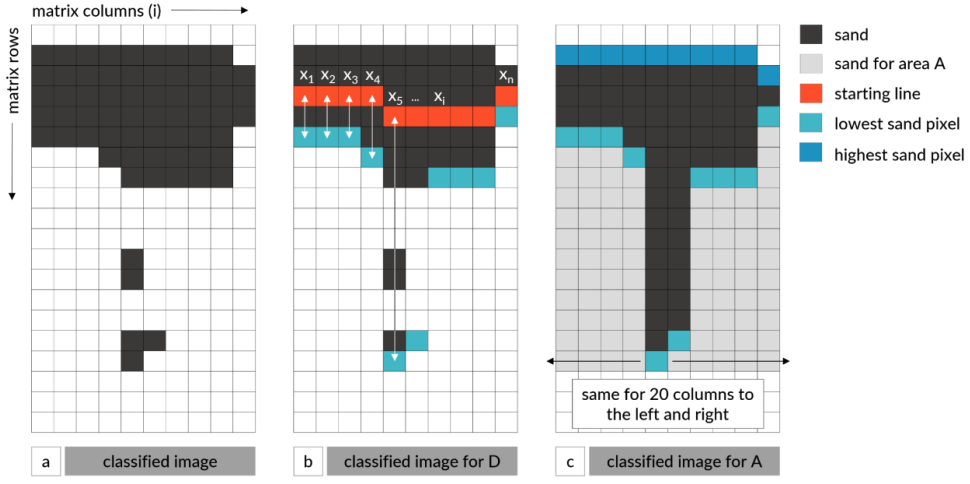


Figure 4: Sketch of the image analysis steps showing a small part of a classified image where each square represents one pixel or element in the matrix (= 1 mm$^2$ on the plot). Pixels classified as sand are shown in black (a). For the determination of the sand distance (D) in every column i the distance ($x_i$) between the starting line (red) and the lowermost sand pixel (turquoise) was determined (b). For the determination of the sand-covered area (A), all pixels between the uppermost (blue) and lowermost sand pixel (turquoise) in each column and the 20 columns to the left and right were considered to be part of area A (c).

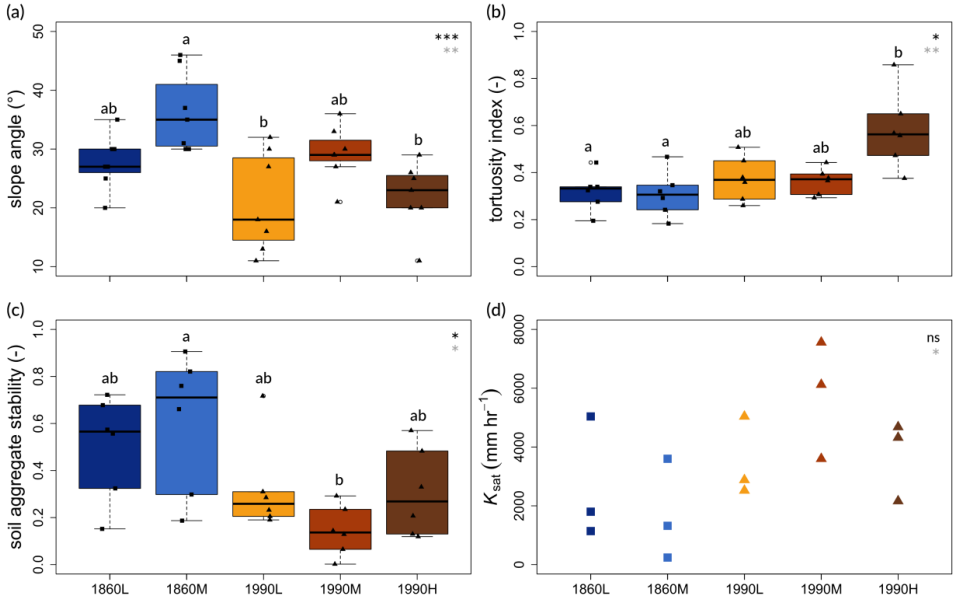


Figure 5: Boxplots of the slope angle (a), tortuosity index (b), and aggregate stability of the top 10 cm of the soil (c), and the saturated hydraulic conductivity ($K_{sat}$) of the soil surface (d) for the five different plots. For the boxplots, the box represents the 25$^{th}$ to 75$^{th}$ percentiles and the solid thick line the median. The whiskers extend to the 10$^{th}$ and 90$^{th}$ percentiles. The jittered symbols represent the actual measurements (squares for the plots on the 1860 moraine and triangles for the plots on the 1990 moraine). The stars in the upper right corner of the plot indicate the level of significance for the differences in median values for the five plots (top in black font), and between the two moraines (bottom in grey font): * for p-values < 0.05, ** for values < 0.01, *** for values < 0.001, and "ns" for p > 0.05. Different letters above the boxplot for the different plots denote a statistically significant difference between the plots.

https://doi.org/10.5194/egusphere-2022-165
Preprint. Discussion started: 21 April 2022


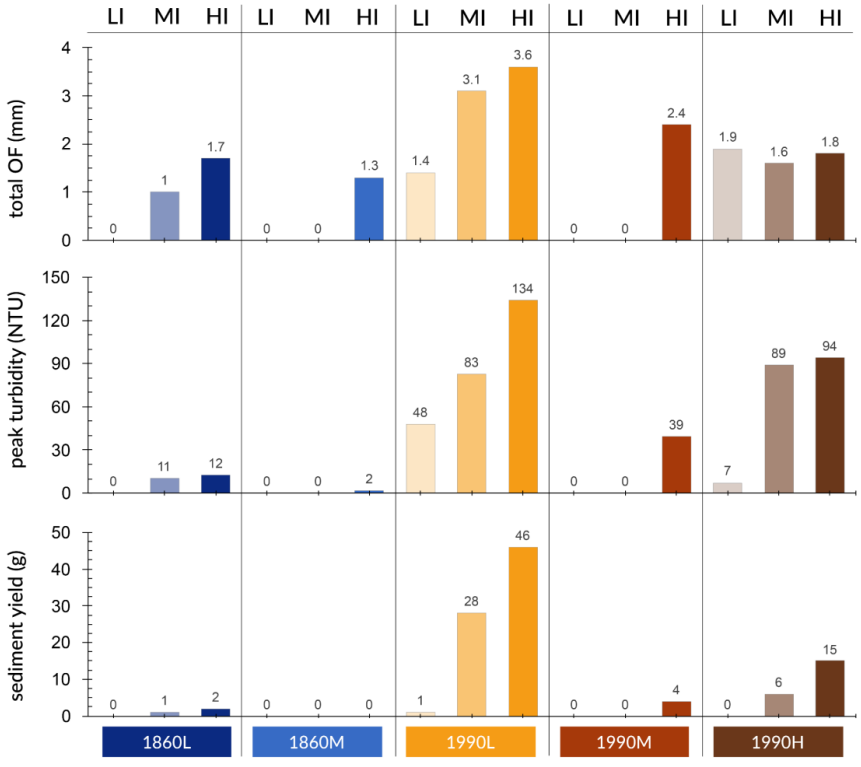


Figure 6: Bar charts of the total amount of OF (mm), peak turbidity (NTU), and the sediment yield (g) for each sprinkling experiment (LI, MI and HI represent low, mid and high intensity experiments, respectively) on each plot (1860L, 1860M, 1990L, 1990M, and 1990H). The absence of a bar indicates the lack of measurable OF (and thus also turbidity and sediment yield). The number above the bar denotes the actual value for each experiment.

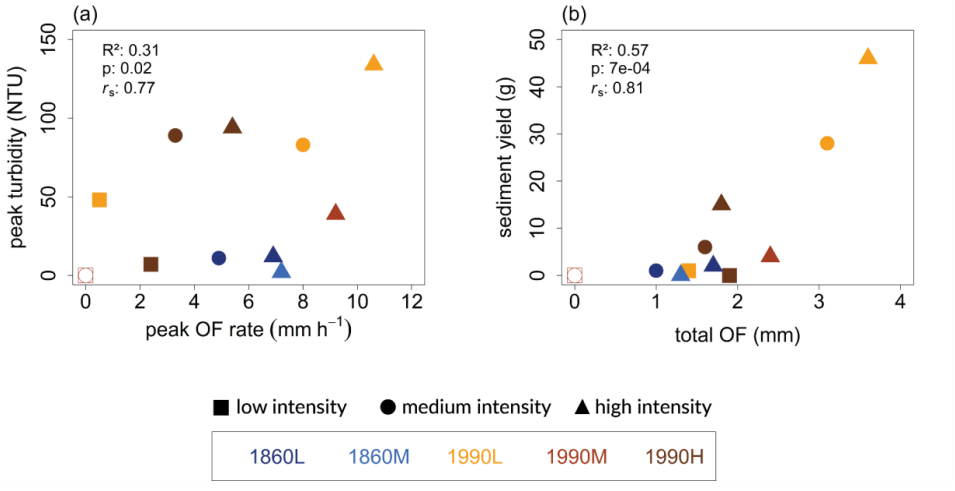


Figure 7: Scatterplots showing the relation between the peak OF rate and peak turbidity (a) and total overland flow and total sediment yield (b) for all sprinkling experiments on the five plots (1860L, 1860M, 1990L, 1990M, and 1990H). The color of the symbols represents the plot; the symbol represents the sprinkling experiment (low (LI), mid (MI), and high (HI) intensity). The coefficient of determination ($R^2$) and corresponding p-value, as well as the Spearman rank correlation coefficients ($r_s$) are given in the upper left corner of each subplot. Note that no OF was measured (and thus also peak OF rate, peak turbidity, and total sediment yield were zero) for five of the 15 experiments, as indicated by the open symbols (i.e., note that only the 1990H LI and MI results are visible because the symbols plot on top of each other).

https://doi.org/10.5194/egusphere-2022-165
Preprint. Discussion started: 21 April 2022


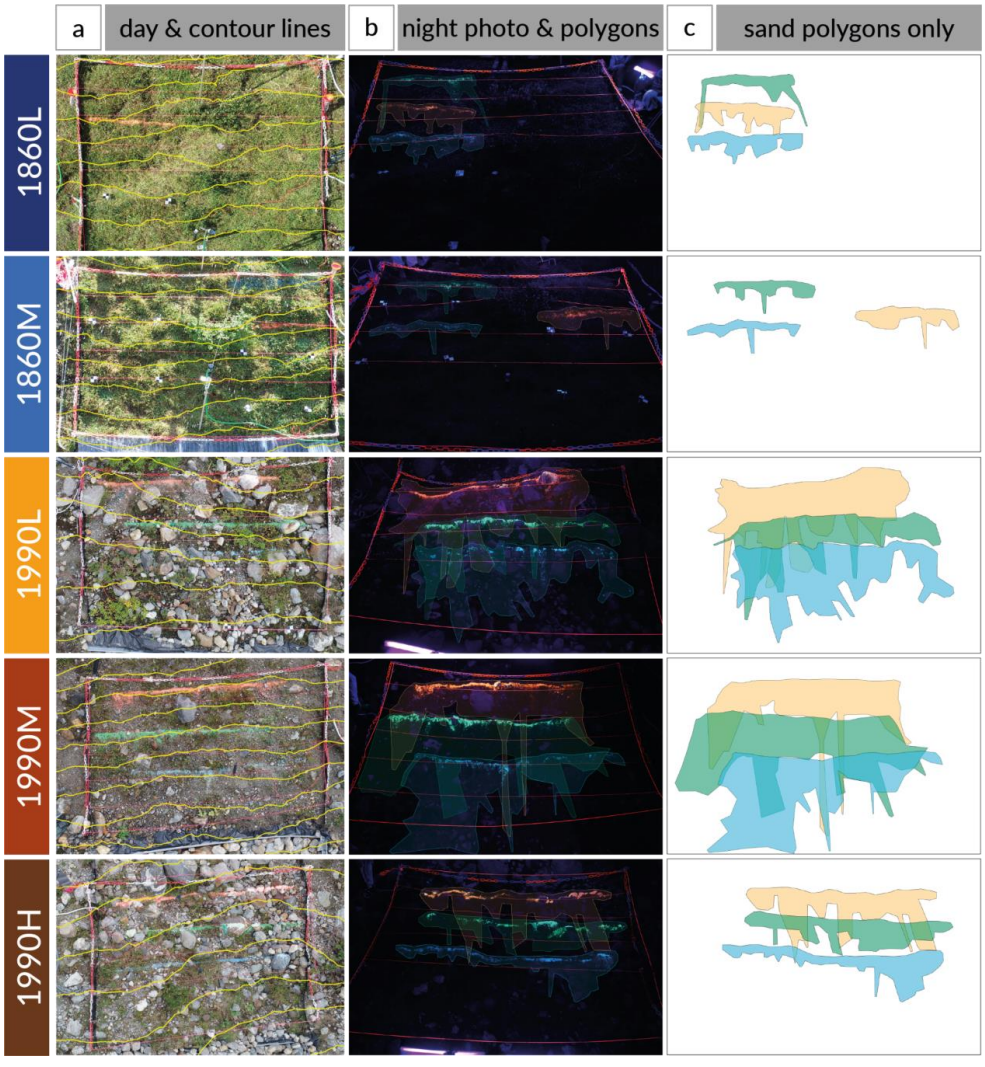


Figure 8: Photographs highlighting the sand-covered areas after the sprinkling experiments for the five plots. The left part of figure (a) shows the daylight drone photos with the 50 cm contour lines (yellow lines). The orange sand ribbon was added prior to the low-intensity experiments (LI), the green sand prior to the medium intensity (MI) experiments, and the blue sand prior to the high intensity (HI) experiments. The central part of figure (b) shows the nighttime photos taken after the experiments while illuminating the fluorescent sand with the UV lamps. To better visualize the extent of the sand movement, hand-drawn polygons (translucent orange: LI experiment, green: MI experiment, and blue: HI experiment) depict the maximum extent of the individual sand particles and clusters, were added to the photos. These polygons are also shown with a white background on the right side of the figure (c). The larger sand-covered areas (and travel distances) for the 1990 plots compared to the 1860 plots are reflected by the larger polygons. The full-size version of the daylight photos with the contour lines and the night photos of the fluorescent sand (without polygons) are given in the Supplementary Material (Figure S1 – S10).

https://doi.org/10.5194/egusphere-2022-165
Preprint. Discussion started: 21 April 2022


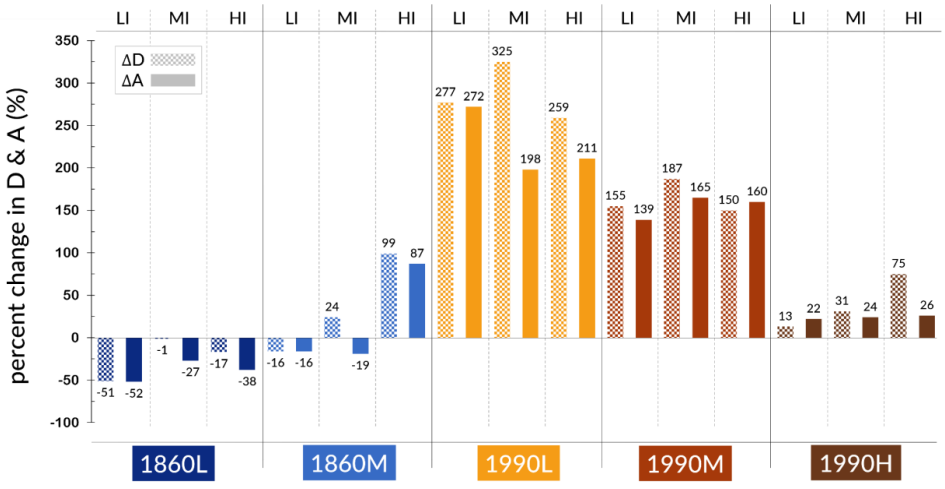


Figure 9: Change in the sand distance (ΔD; shaded bars) and sand-covered area (ΔA; solid bars) between pre- and post-sprinkling conditions for all experiments on all five plots. LI, MI and HI represent low, medium and high-intensity sprinkling experiments. Positive changes reflect increases in sand distances and areas during the experiment and thus sand movement and deposition on the surface below the sand ribbon, while negative changes reflect a loss of sand from the surface.

https://doi.org/10.5194/egusphere-2022-165
Preprint. Discussion started: 21 April 2022


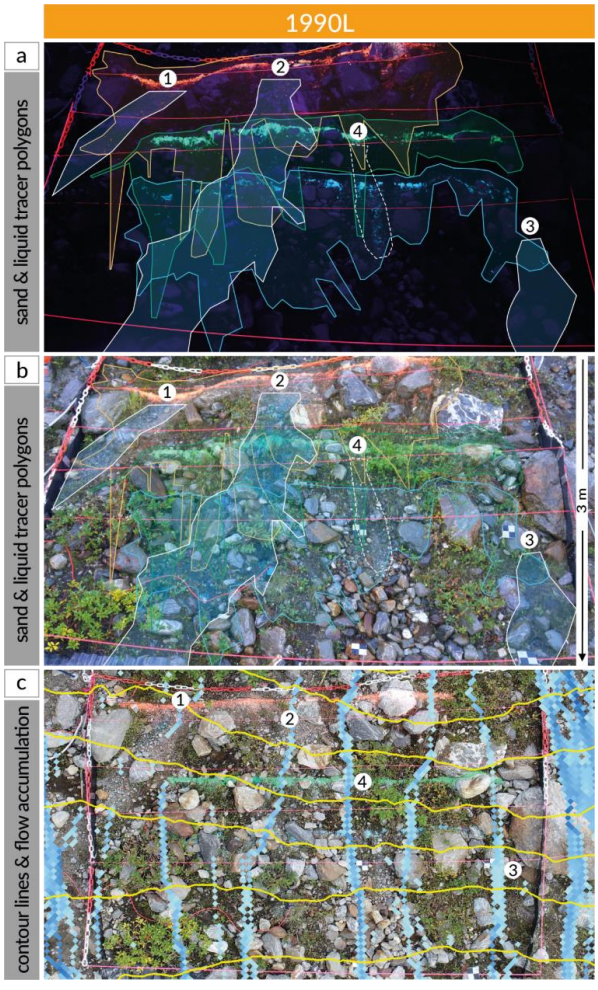


Figure 10: Overland flow (OF) pathways and sand-covered areas after the sprinkling experiments for the low complexity plot on the 1990 moraine (1990L). The upper photo (a) was taken at night with the hand-drawn polygons (from Figure 8) to visualize the distribution of the sand. The orange, green and blue polygons indicate the sand-covered areas on the plot. The white polygons indicate OF pathways that were either clearly visible (#4) or traced by adding a brilliant blue tracer (#1, #2, #3) to the water. The middle picture (b) is a composite of several video frames from the MI and HI experiments after the addition of the blue dye to visualize the OF pathways on the plot, again with the polygons. The lower figure (c) shows a nadir view of the plot surface and includes the 50 cm contour lines (yellow lines) and the $D_\infty$ derived flow accumulation (values larger than 0.2 $m^2$ in blue). Numbers 1 – 4 reflect specific flow pathways described in the text.

https://doi.org/10.5194/egusphere-2022-165
Preprint. Discussion started: 21 April 2022


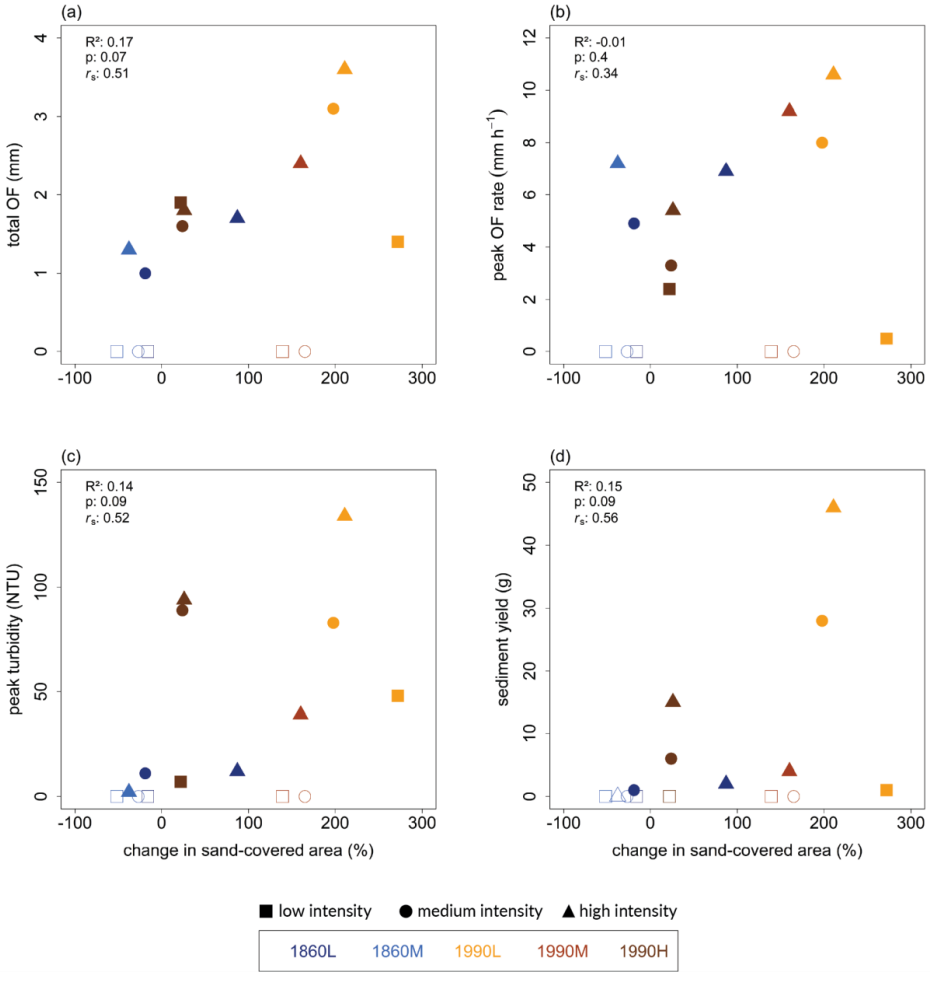


Figure 11: Scatterplots showing the relations between the change in sand-covered area (ΔA) and total overland flow (OF; a), peak flow rate (b), peak turbidity (c) and total sediment yield (d) for all sprinkling experiments. The color of the symbols represents the plots (1860L, 1860M, 1990L, 1990M, 1990H); the symbol represents the rainfall intensity of the sprinkling experiment (LI, MI, HI). Open symbols are used for experiments that did not generate any OF at the bottom of the plot (and thus no turbidity and sediment yield). The coefficient of determination ($R^2$) and corresponding p-value, as well as the Spearman rank correlation coefficient ($r_s$) are given in the upper left corner of each subplot. The results for ΔD are similar and shown in the Supplementary Material (Figure S11).